Figures from

Digital Signal Compression: Principles and Practice

William A. Pearlman and Amir Said

List of Figures

Chapter 1

Motivation

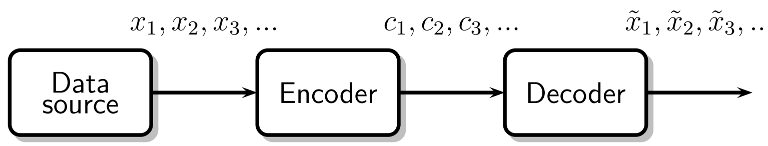

Figure 1.1: Basic data encoding and decoding model.

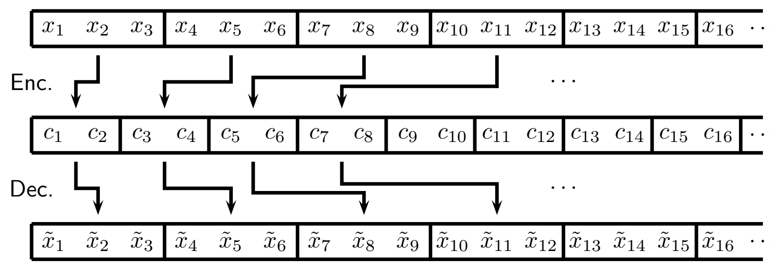

(a) Fixed-to-fixed coding.

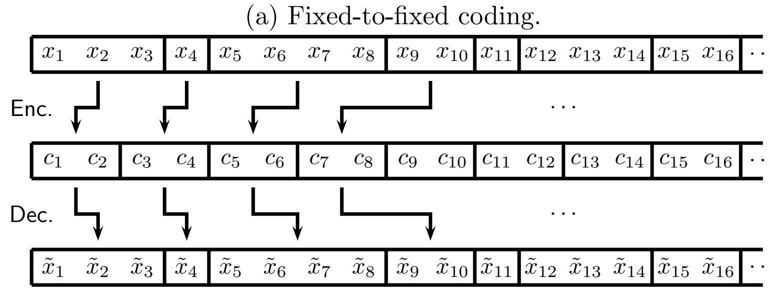

(b) Variable-to-fixed coding.

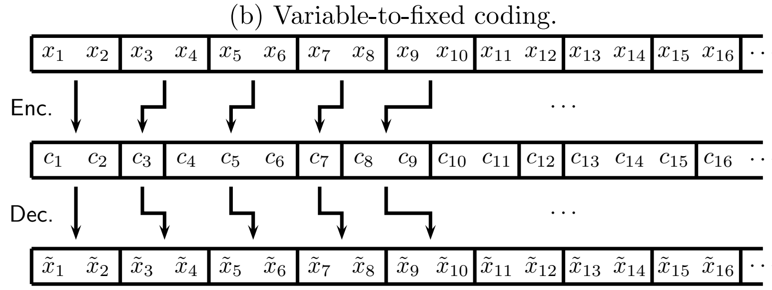

(c) Fixed-to-variable coding.

Figure 1.2: Example of some forms in which the source and compressed data symbols can be organized for compression.

Chapter 2

Book Overview

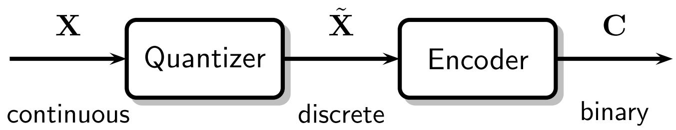

Figure 2.1: Source letter quantization followed by binary coding.

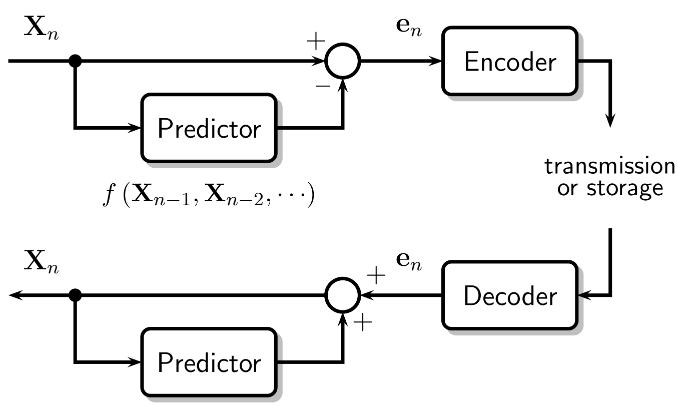

Figure 2.2: Lossless predictive coding system: top is encoder; bottom is decoder.

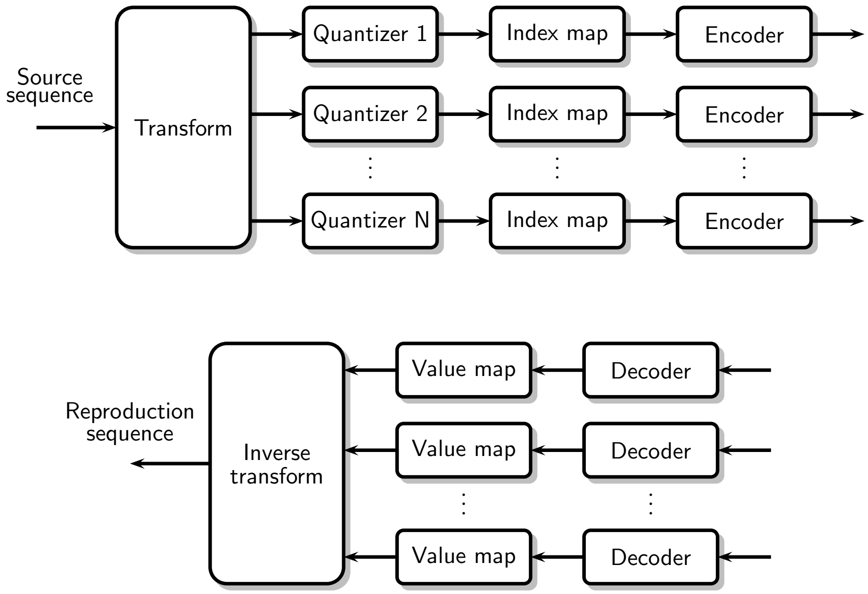

Figure 2.3: Transform coding system: encoder on top; decoder at bottom.

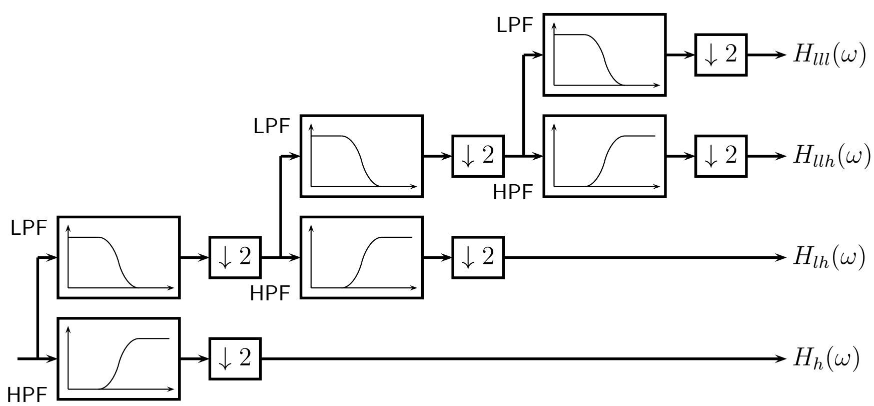

Figure 2.4: Example of how lowpass (LPF) and highpass (HPF) filters can be used for computing the subband transform.

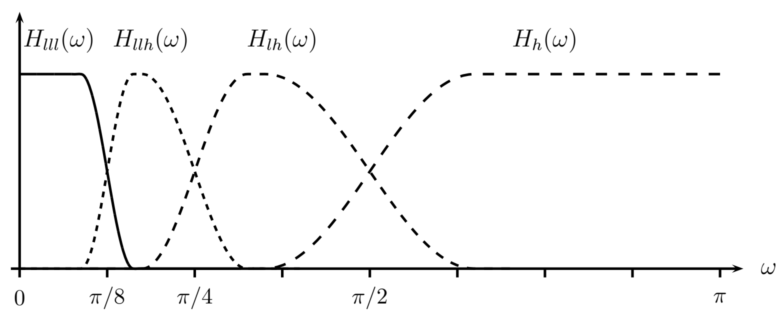

Figure 2.5: Example of a type of frequency response produced by filters used in the subband transform.

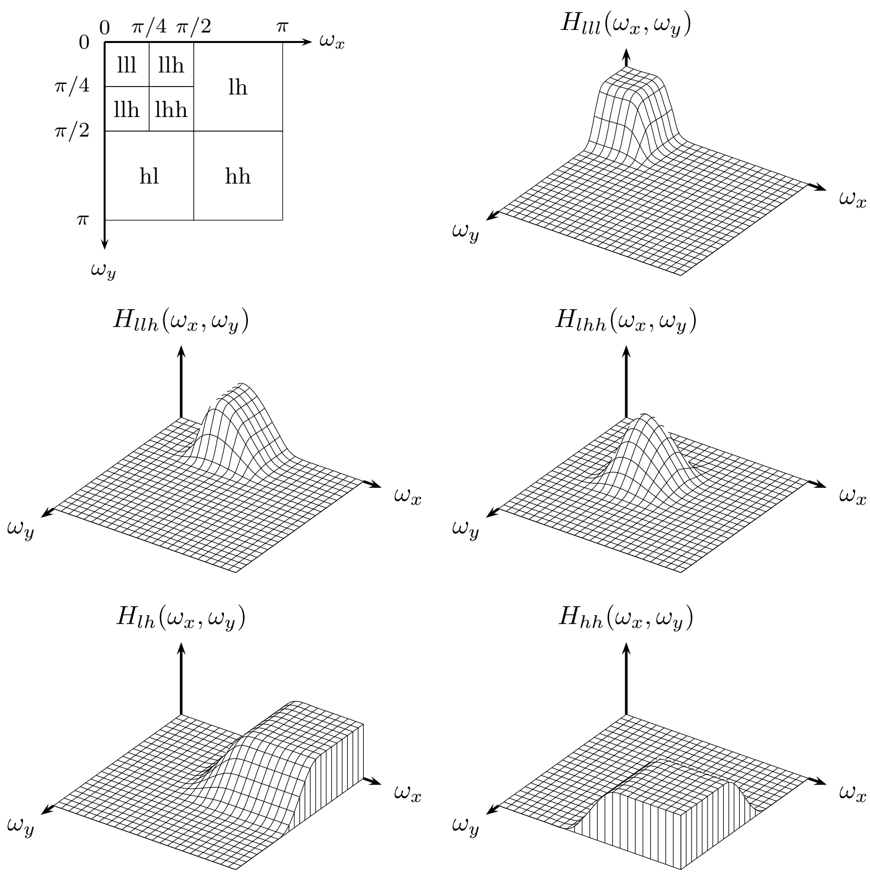

Figure 2.6: Example logical division of subbands (top-left) and types of frequency response produced by some of the filters used in the two-dimensional subband transform.

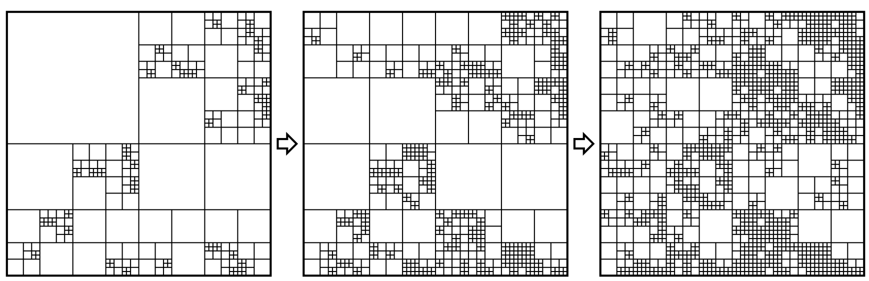

Figure 2.7: Example of how a set of image pixels is sequentially subdivided for more efficient compression using set partition coding.

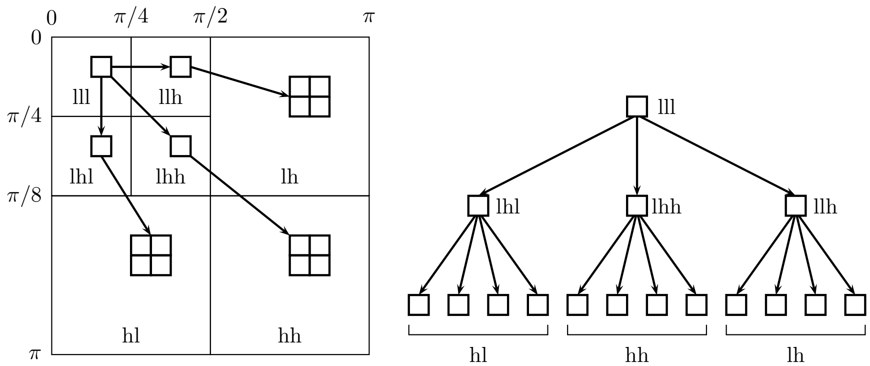

Figure 2.8: Transform coefficients in spatial frequency wavelet subbands (left) are organized to form spatial orientation trees (SOTs, right).

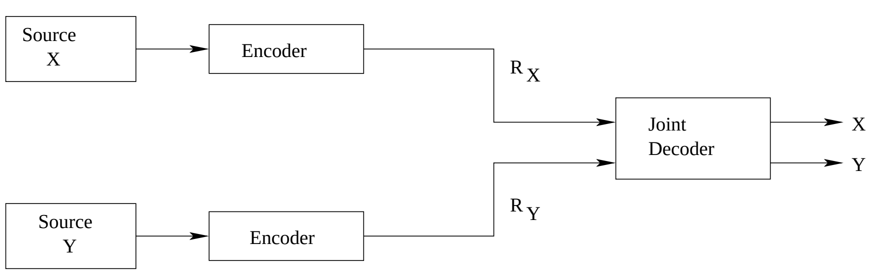

Figure 2.9: Distributed source coding: independent encoding and joint decoding of correlated sources.

Chapter 3

Principles of Lossless Compression

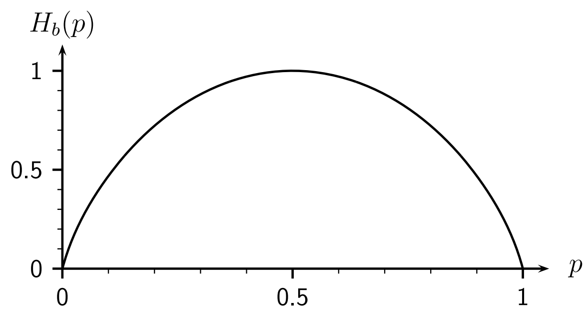

Figure 3.1: The binary entropy function.

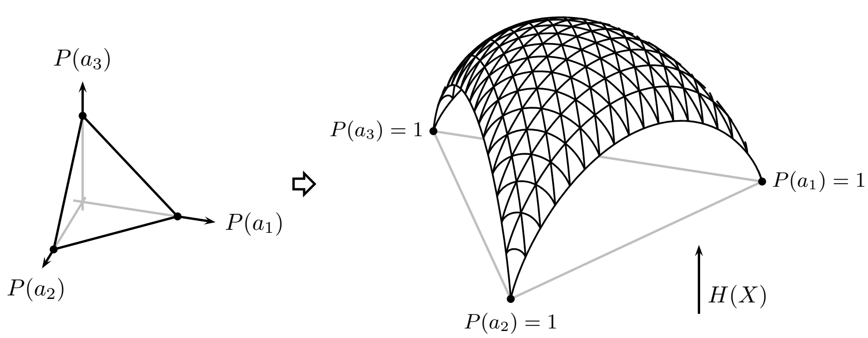

Figure 3.2: The entropy function for source alphabets with three symbols.

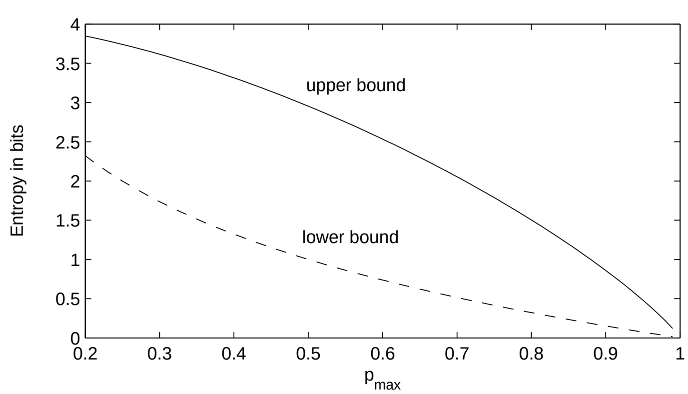

Figure 3.3: Upper and lower bounds on the entropy function. Solid line corresponds to Eq. (3.10) for $K = 16$ and dashed line to Eq. (3.11).

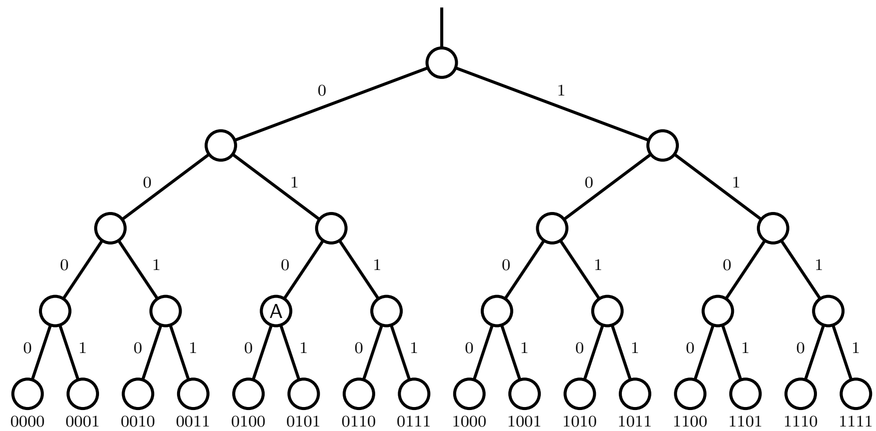

Figure 3.4: A binary tree.

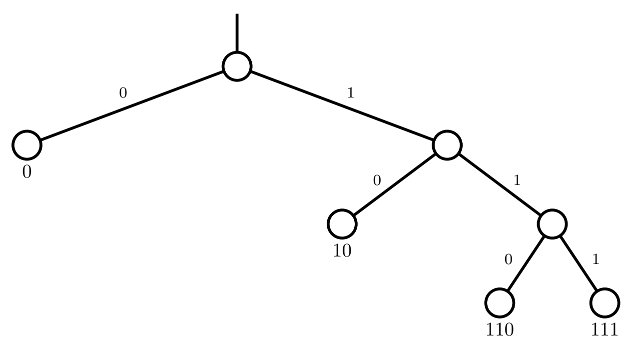

Figure 3.5: The code tree for binary code in Table 3.1.

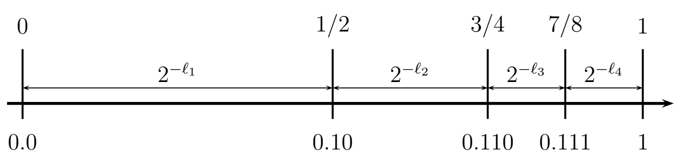

Figure 3.6: Binary code construction for lengths $\ell_1 = 1, \ell_2 = 2, \ell_3 = 3, \ell_4 = 3$ by association to binary fractions.

Chapter 4

Entropy Coding Techniques

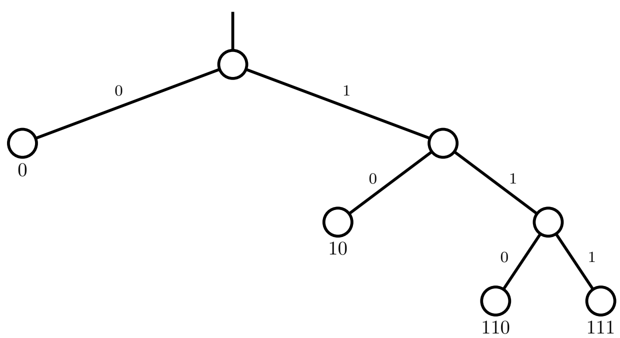

Figure 4.1: The code tree for binary code in Table 4.1.

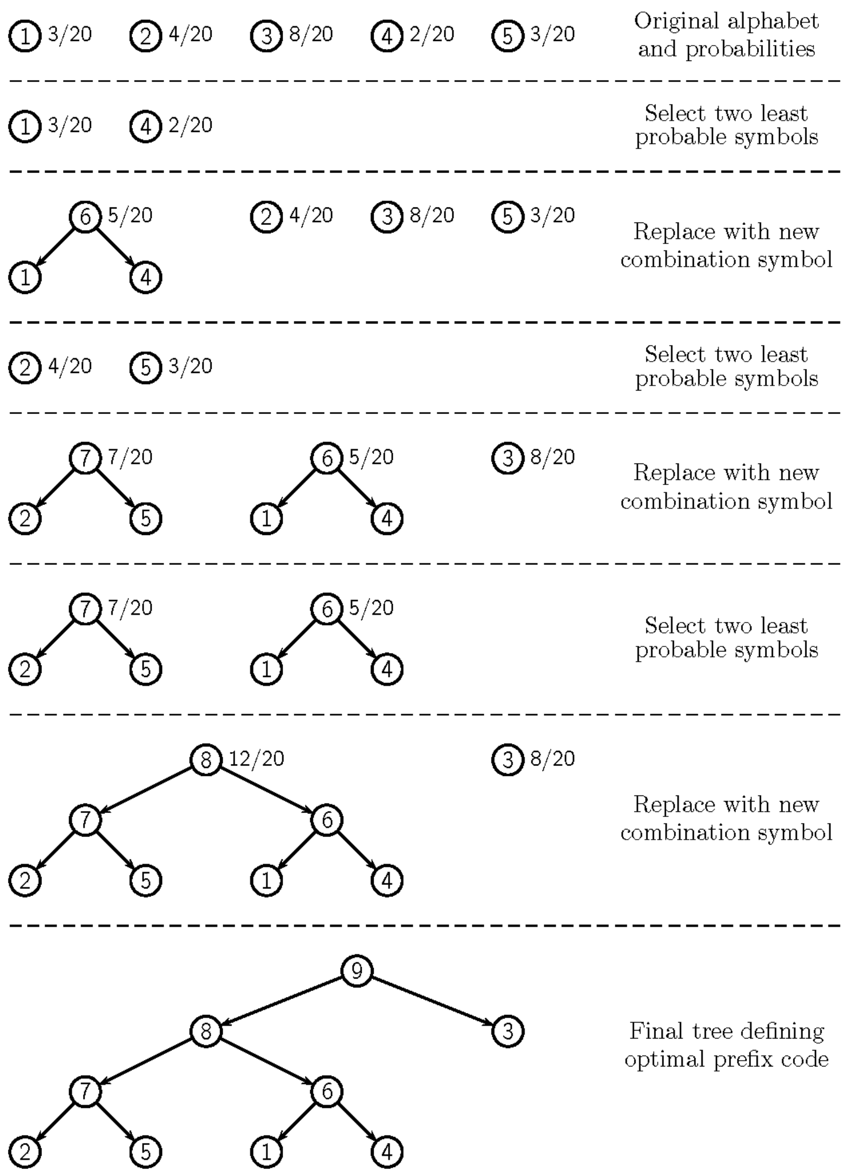

Figure 4.2: The Huffman coding procedure.

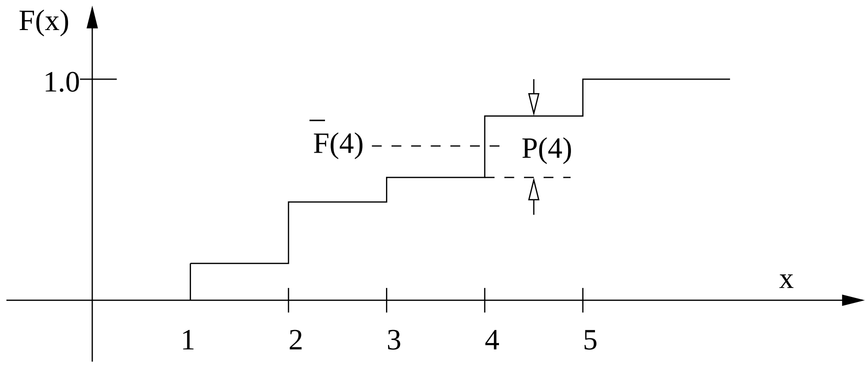

Figure 4.3: CDF graph for $K = 5$ letters.

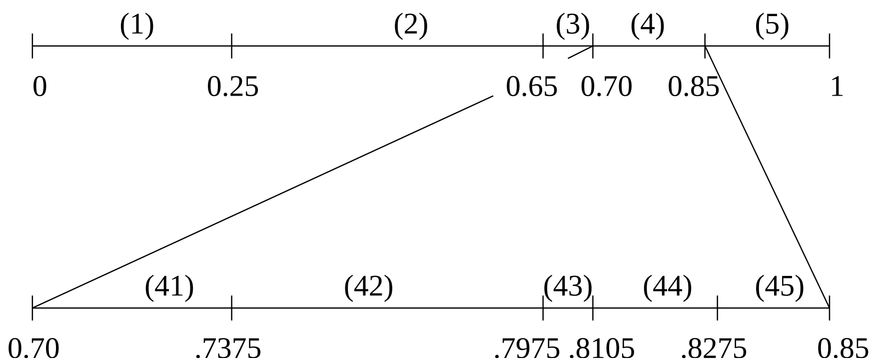

Figure 4.4: Mapping sequences to intervals in arithmetic coding.

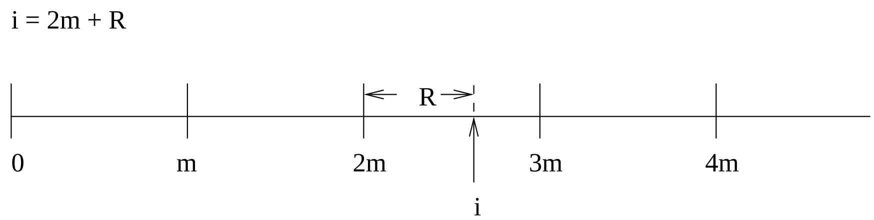

Figure 4.5: Illustration of number representation for Golomb coding.

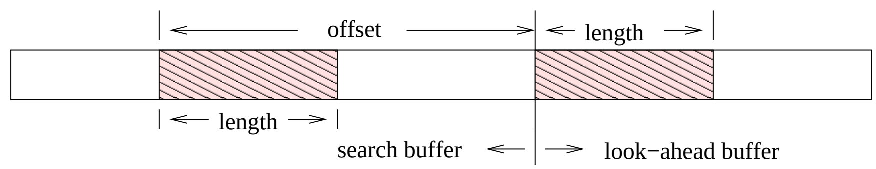

Figure 4.6: Buffer and pointer definitions in LZ77 coding.

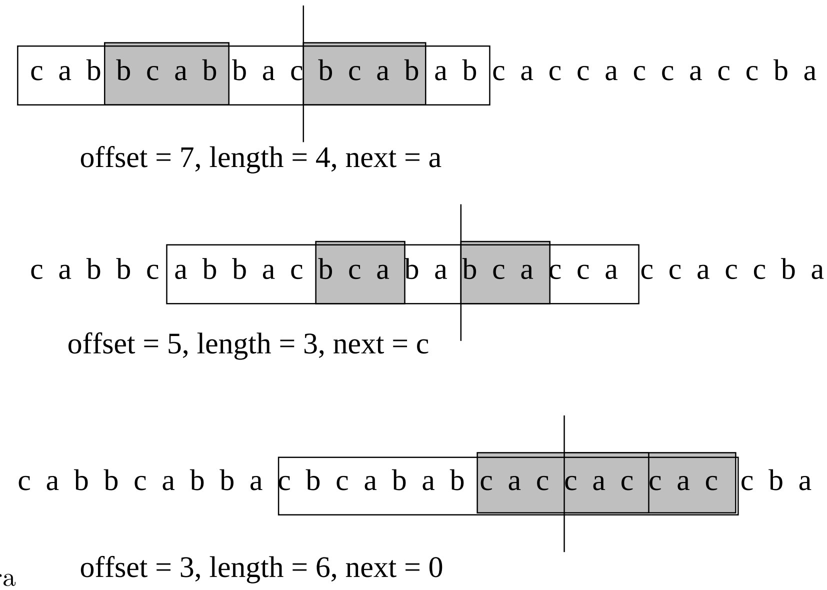

stra

Figure 4.7: Example of first three stages of LZ77 coding.

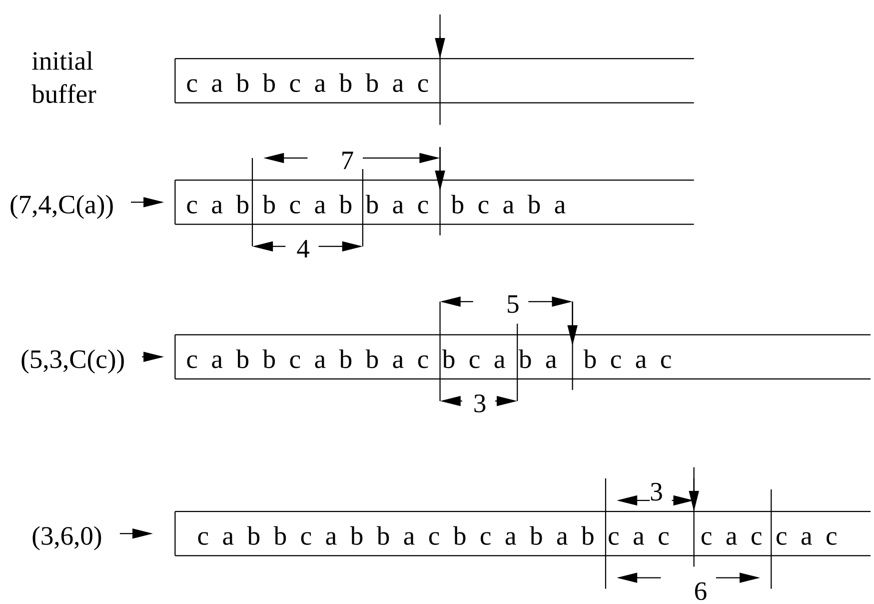

Figure 4.8: Example of first three stages of LZ77 decoding.

Chapter 5

Lossy Compression of Scalar Sources

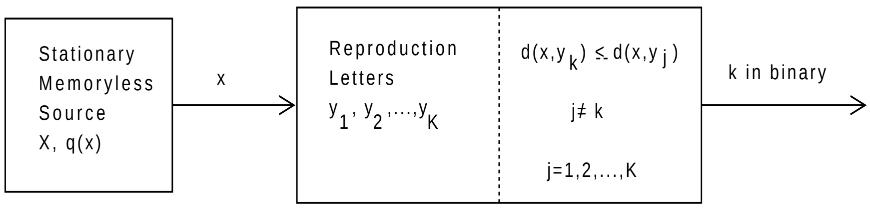

Figure 5.1: Model of scalar quantization.

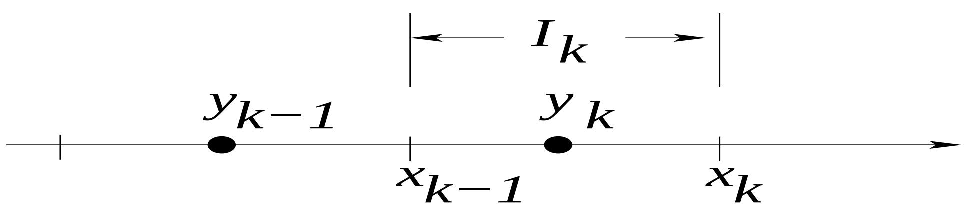

Figure 5.2: Threshold and reproduction points and intervals.

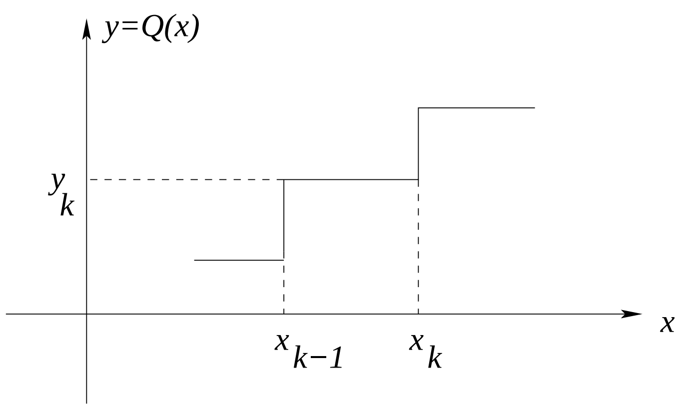

Figure 5.3: Graphical form of quantizer function.

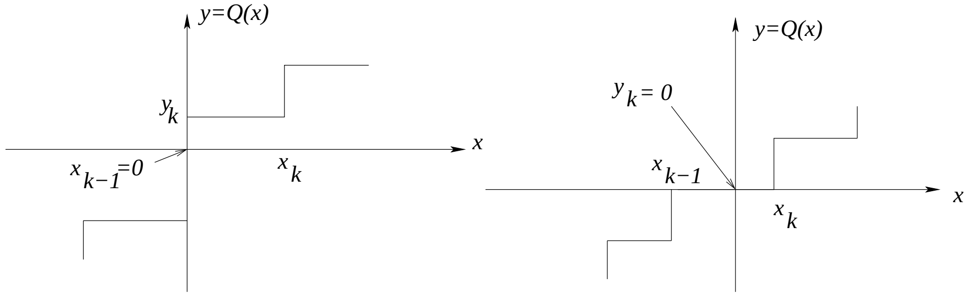

Figure 5.4: Mid-rise (left) and mid-tread (right) quantizer functions.

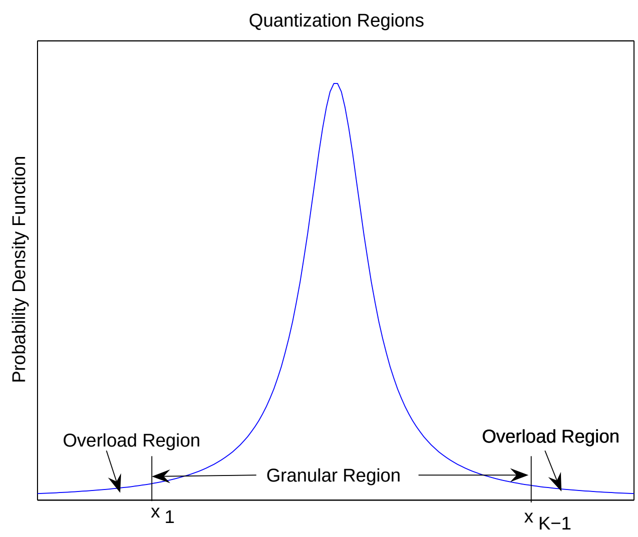

Figure 5.5: Depiction of overload and granular regions with respect to a probability density function.

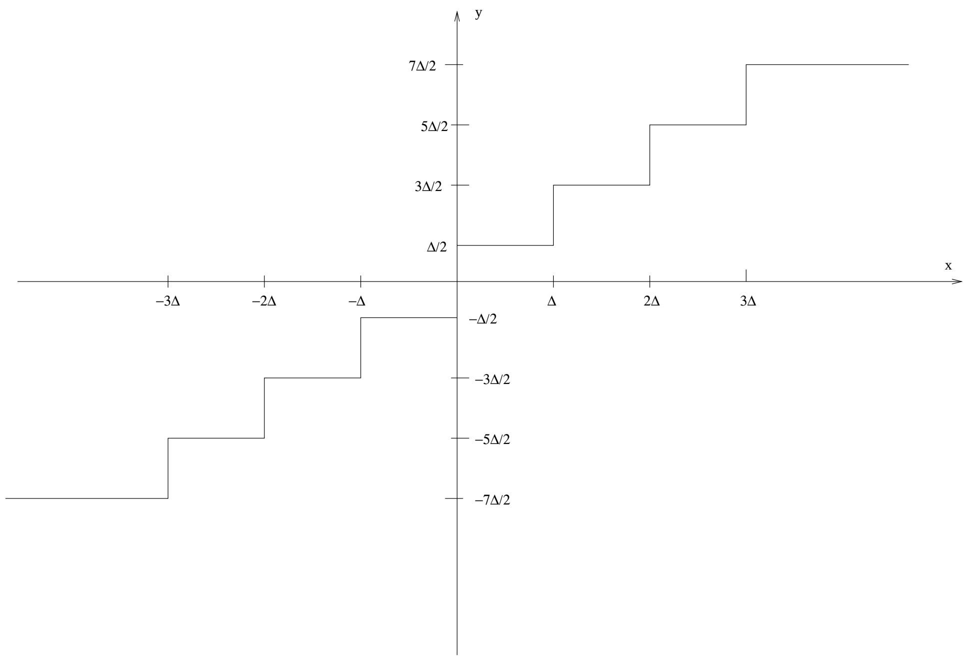

Figure 5.6: Mid-rise uniform quantizer characteric for $K = 8$ quantization levels.

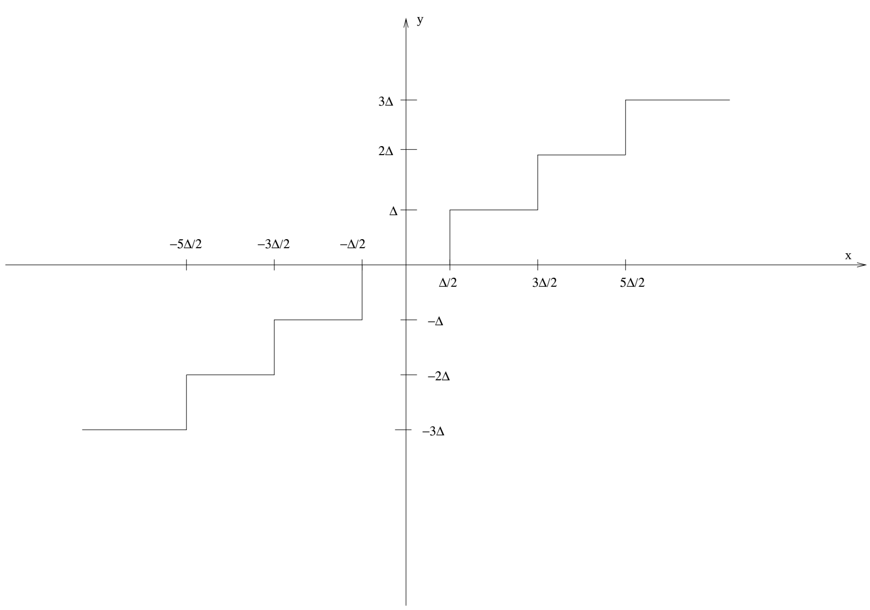

Figure 5.7: Mid-tread quantizer characteric for $K = 7$ quantization levels.

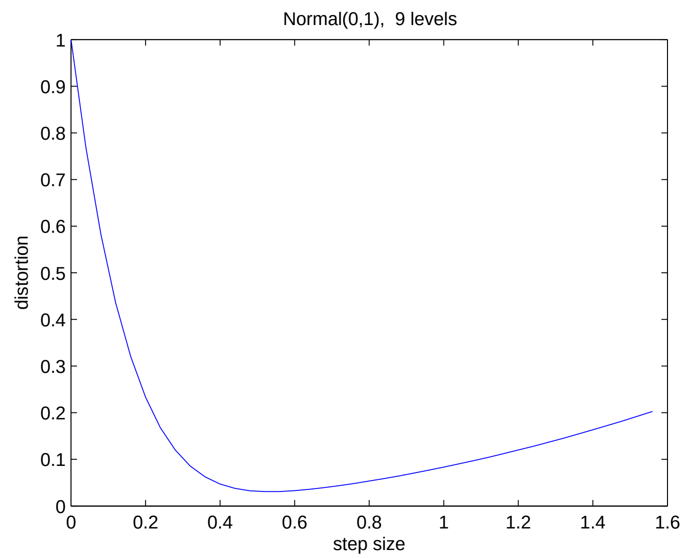

Figure 5.8: Mean squared error versus step size for uniform quantization of a Normal(0,1) source with $K = 9$ quantization levels.

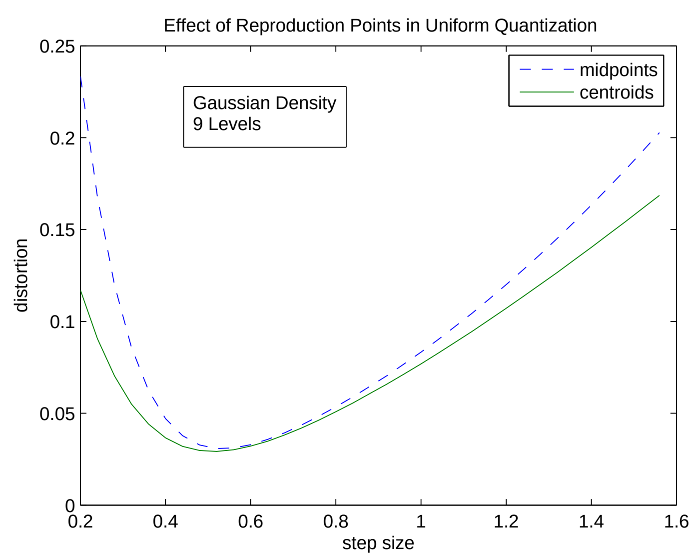

Figure 5.9: Distortion of midpoint versus centroid reproduction points for quantization of a Normal(0,1) source with $K = 9$ quantization levels.

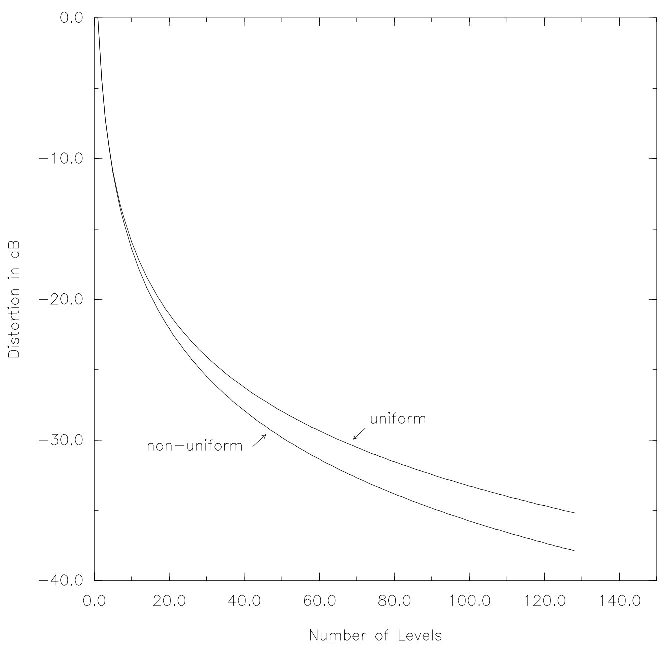

Figure 5.10: Uniform and non-uniform quantization of a unit variance Gaussian probability density.

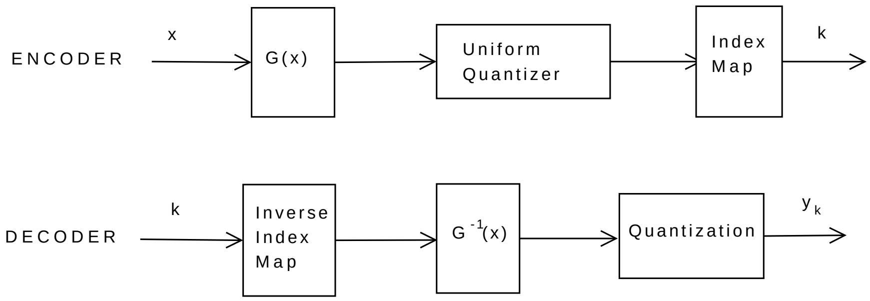

Figure 5.11: A companding quantization system.

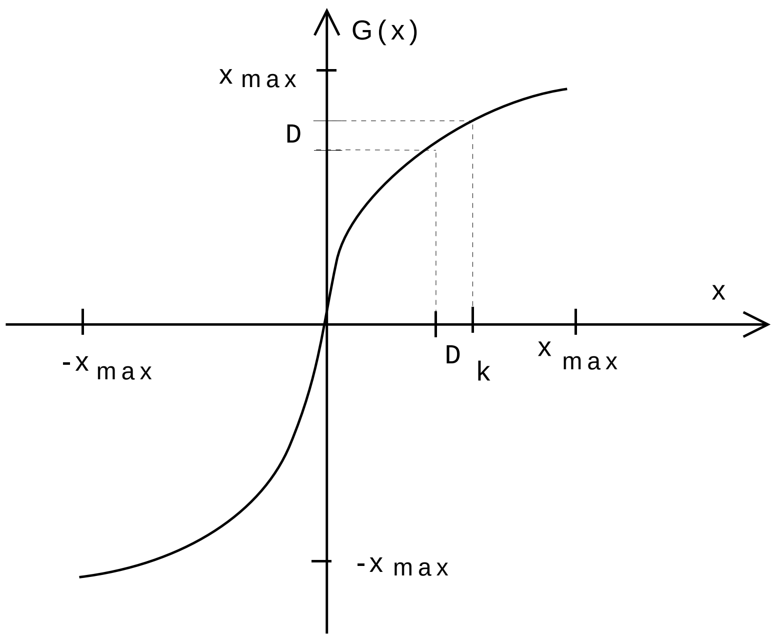

Figure 5.12: A companding quantization system.

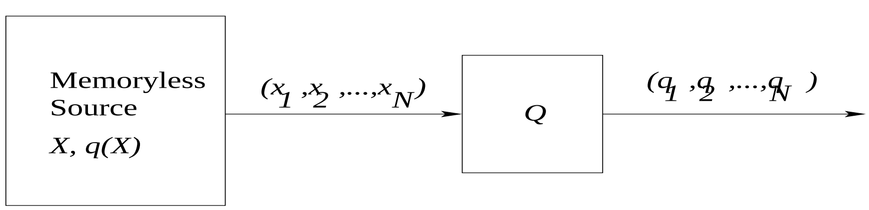

Figure 5.13: Quantization of a sequence from the source.

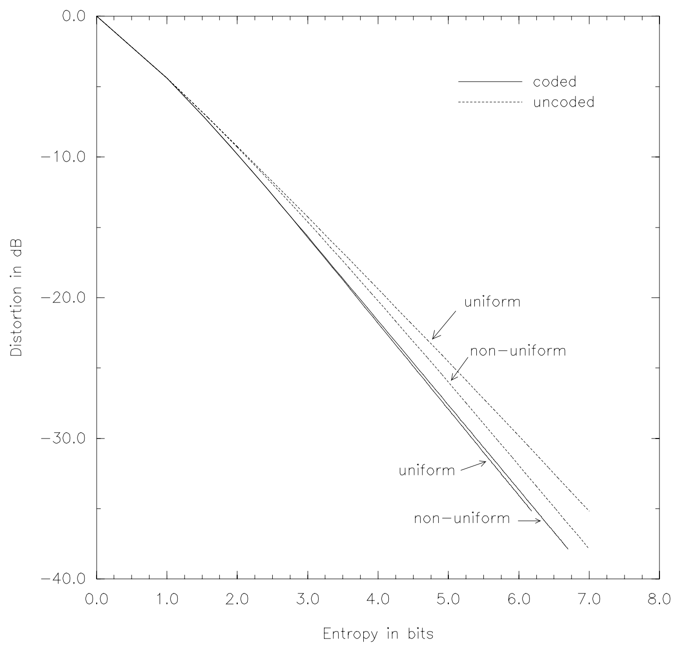

Figure 5.14: Comparison of uncoded and entropy-coded quantization for non-uniform and uniform quantizer levels. The source is the unit variance Gaussian and the distortion is squared error.

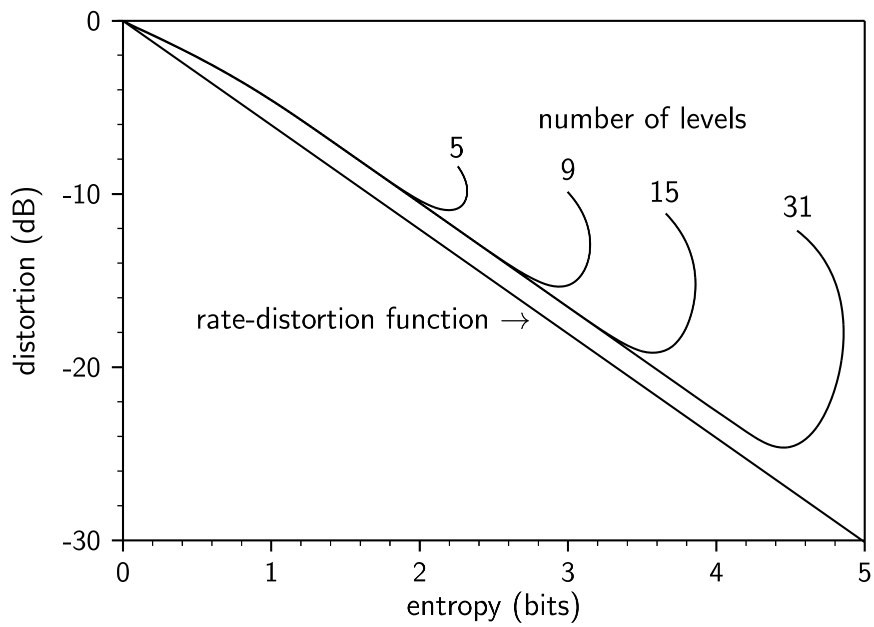

Figure 5.15: Mean squared error versus entropy for different numbers of levels in uniform quantization.

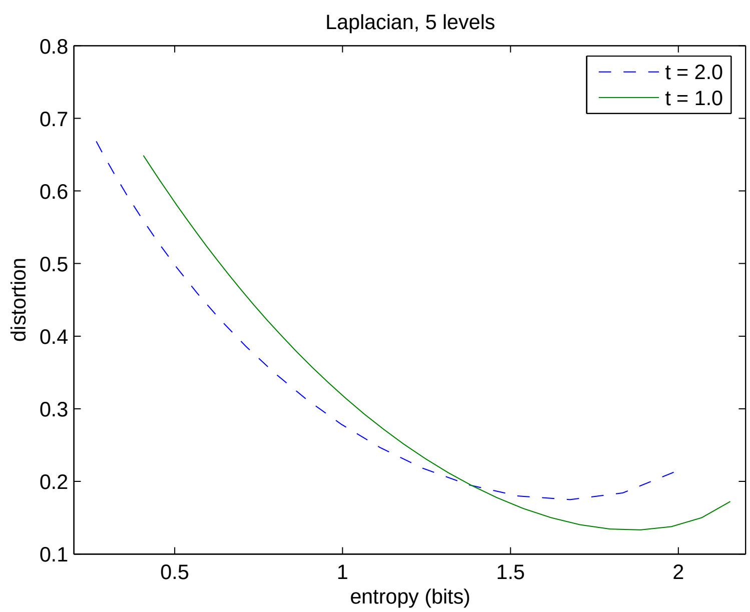

Figure 5.16: Double and normal null zone widths in 5-level uniform quantization of a Laplacian probability density with zero mean and unit variance.

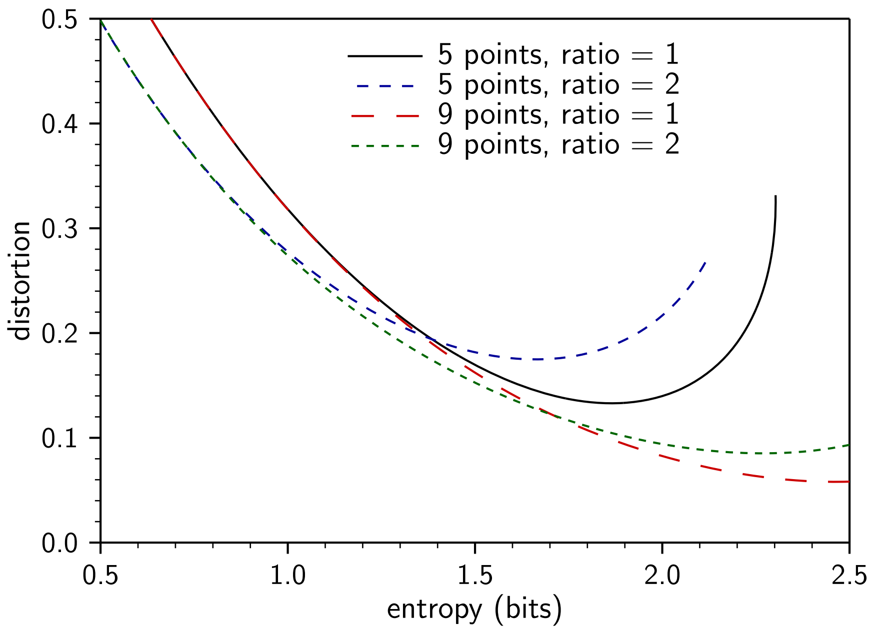

Figure 5.17: Mean squared error versus entropy for 5 and 9 quantization levels with normal (ratio = 1) and double (ratio = 2) null zone. The probability density function is Laplacian with zero mean and unit variance. The reproduction points are the mid-points of the uniform width decision intervals (quantizer bins).

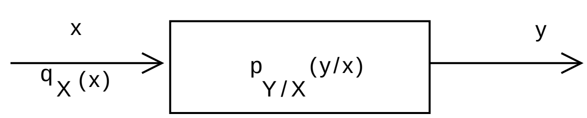

Figure 5.18: A test channel.

Chapter 6

Coding of Sources with Memory

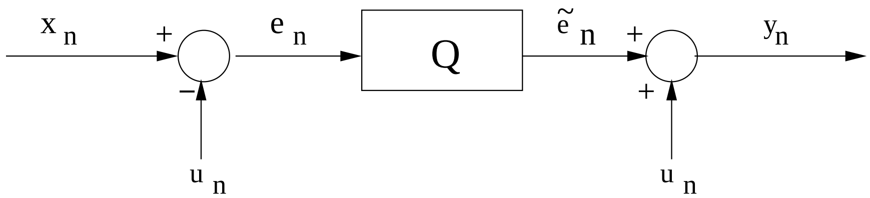

Figure 6.1: Depiction of subtraction and addition of same quantity before and after quantization (Q), whereby reconstruction error equals quantization error.

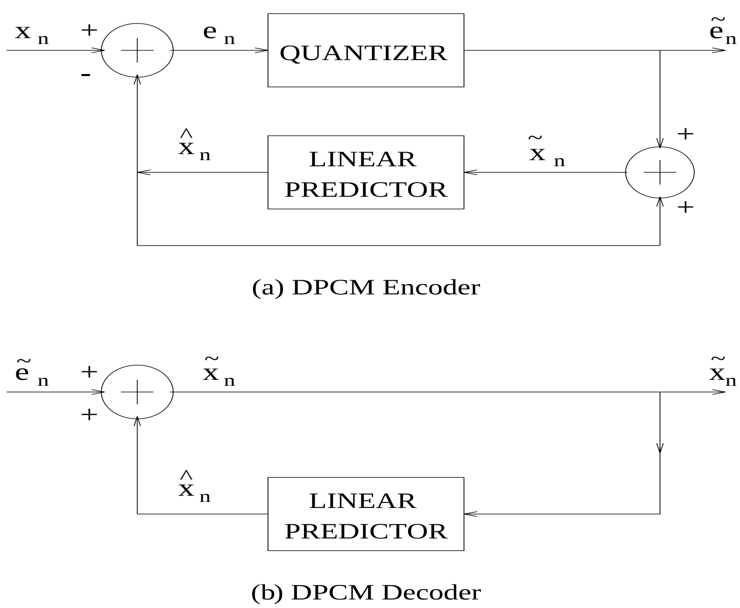

Figure 6.2: DPCM encoder and decoder.

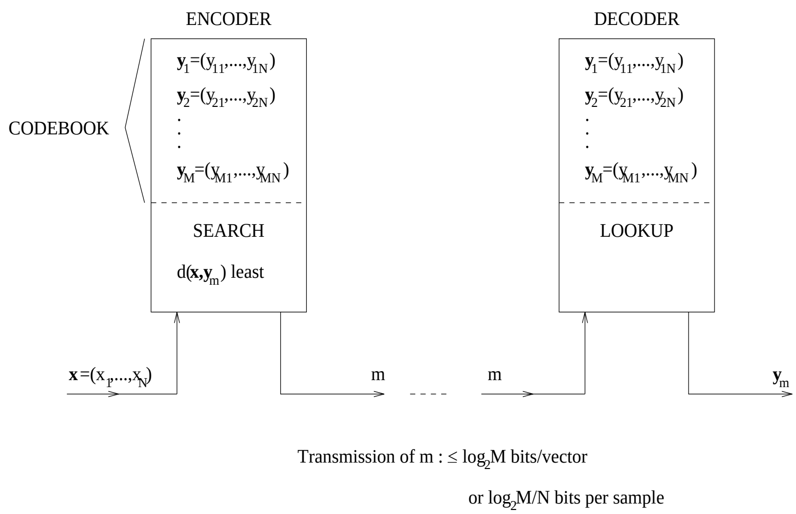

Figure 6.3: A block or vector coding system model.

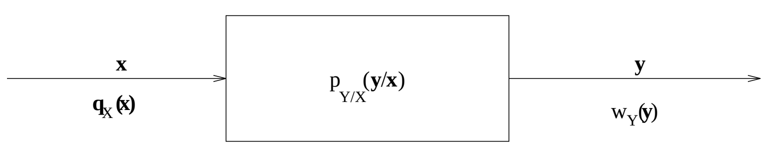

Figure 6.4: A test channel.

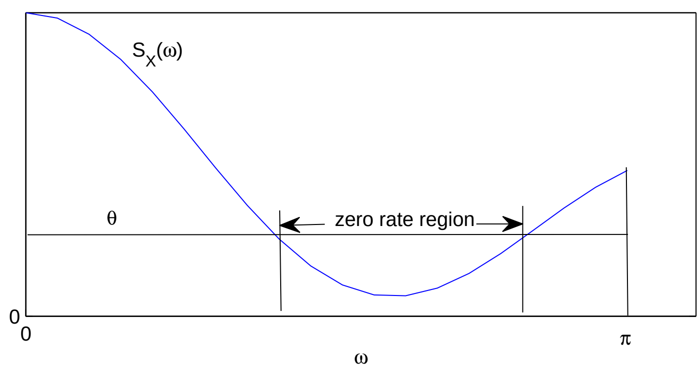

Figure 6.5: Continuous spectral density and parameter level θ dictating the optimal rate assignment versus frequency.

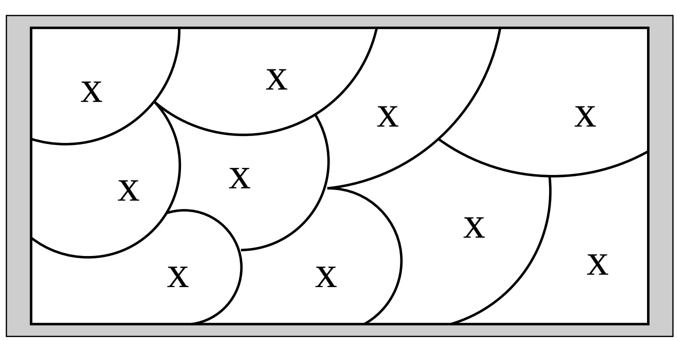

Figure 6.6: Decision regions and their reproduction points marked by 'X' for a hypothetical two-dimensional vector quantizer.

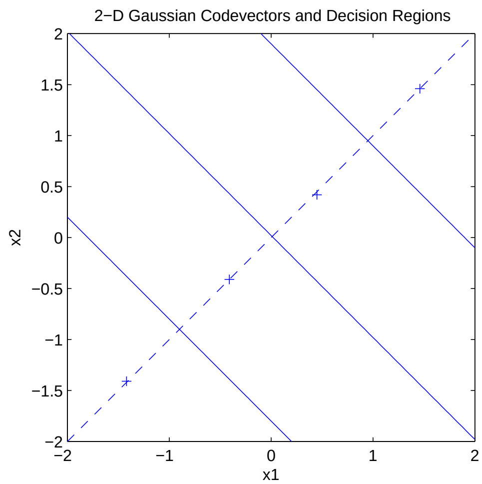

Figure 6.7: Codevectors and decision regions in range $-2 \leq x_1, x_2 \leq 2$ for two-dimensional Gaussian, $\rho = 0.9$, quantizer in example.

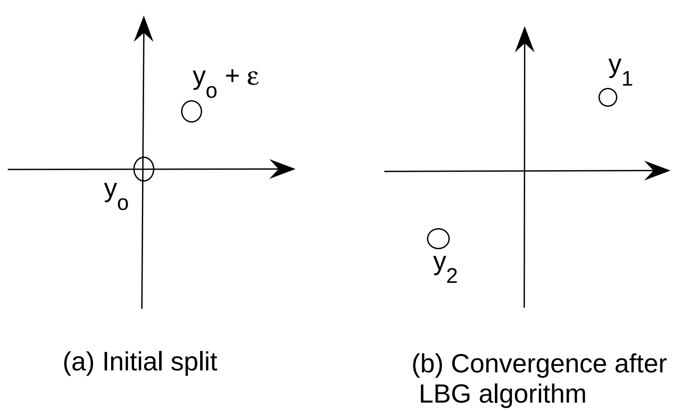

Figure 6.8: (a) Binary splitting of covectors. (b) Convergence to two best codevectors.

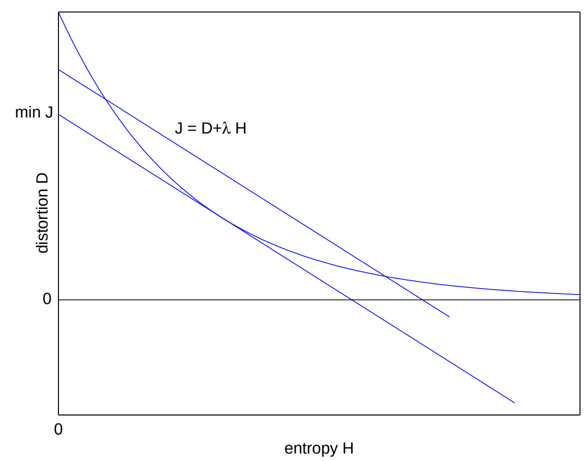

Figure 6.9: Depiction of the objective minimum of an entropy-constrained vector quantizer.

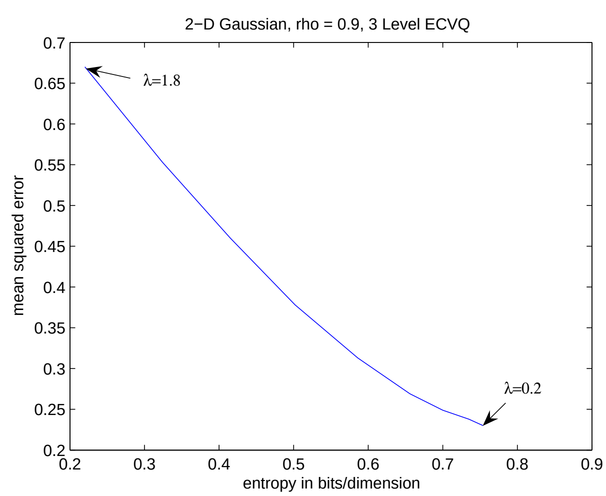

Figure 6.10: MSE versus entropy for two-dimensional Gaussian, $\rho = 0.9$, 3-level quantizer.

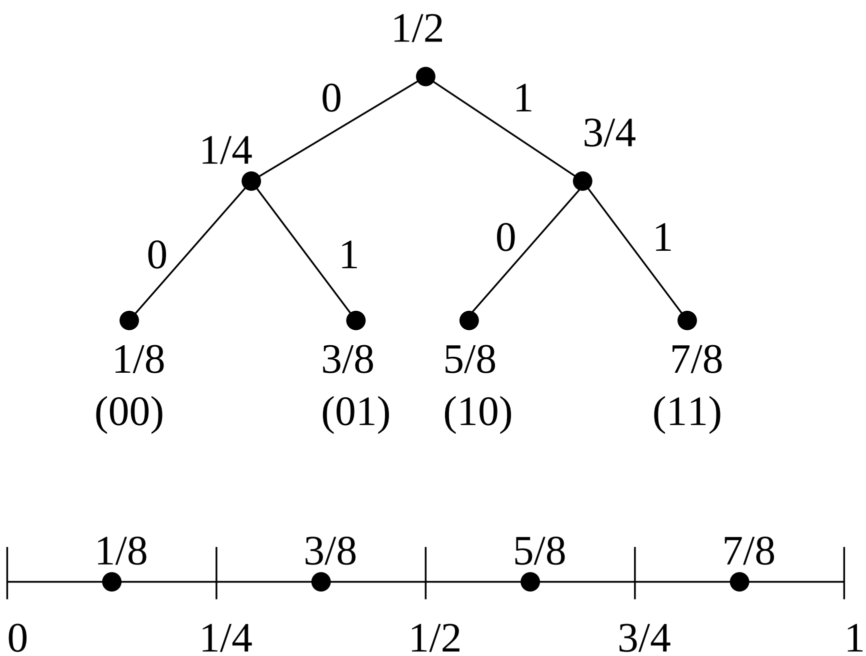

Figure 6.11: Quantization points, decision intervals, and binary tree for uniform quantization in the interval [0,1).

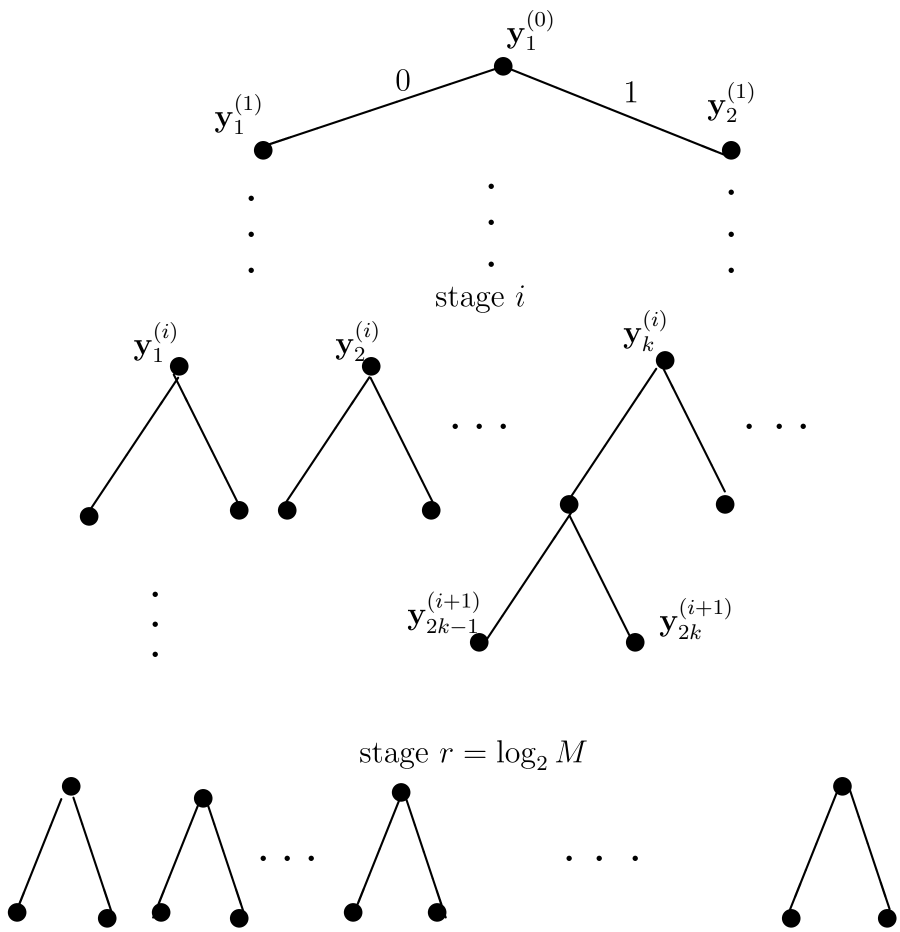

Figure 6.12: Tree-structured VQ design. Bottom nodes contain $M = 2^r$ code-vectors of the codebook.

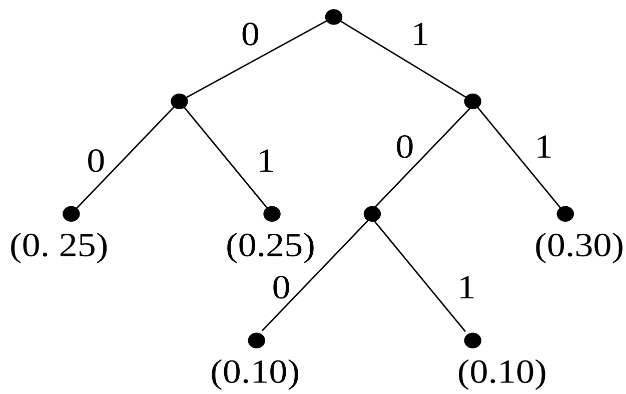

Figure 6.13: Example of unbalanced tree in TSVQ. The numbers in parentheses at the terminal nodes are the probabilities of the codevectors (or codewords) associated with these nodes.

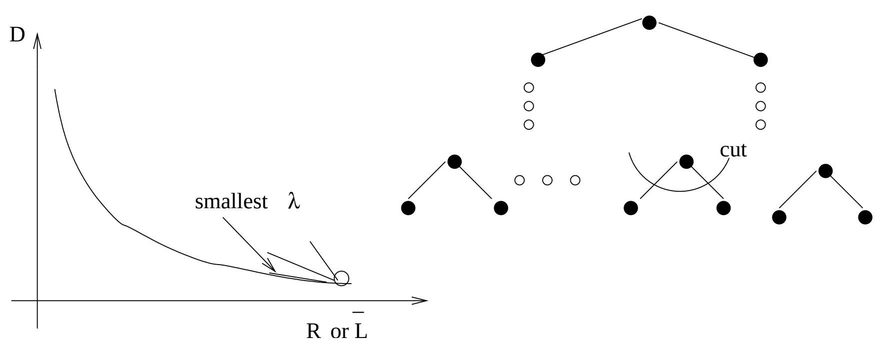

Figure 6.14: Example of first pruning of TSVQ tree and selection of smallest λ in distortion-rate curve. .

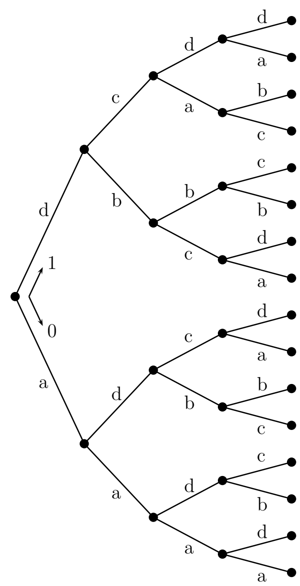

Figure 6.15: Four initial stages of a rate $R = 1$ bit/source letter code tree.

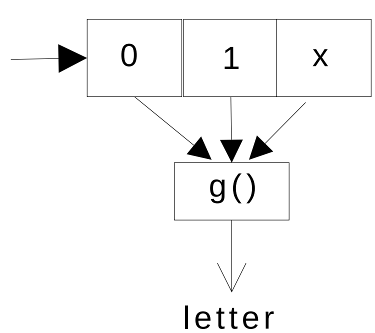

Figure 6.16: Finite-state machine realization of a four-state rate $R = 1$ bit per source letter code in state $\boxed{10}$.

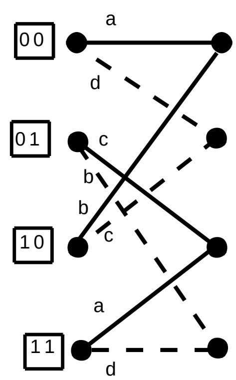

Figure 6.17: One stage trellis depicting state transitions and outputs of finite-state machine code in Fig. 6.16.

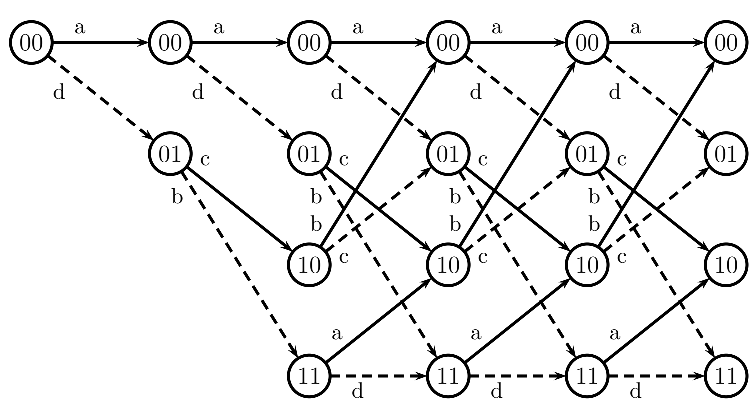

Figure 6.18: Trellis of a four-state rate $R = 1$ bit per source letter code.

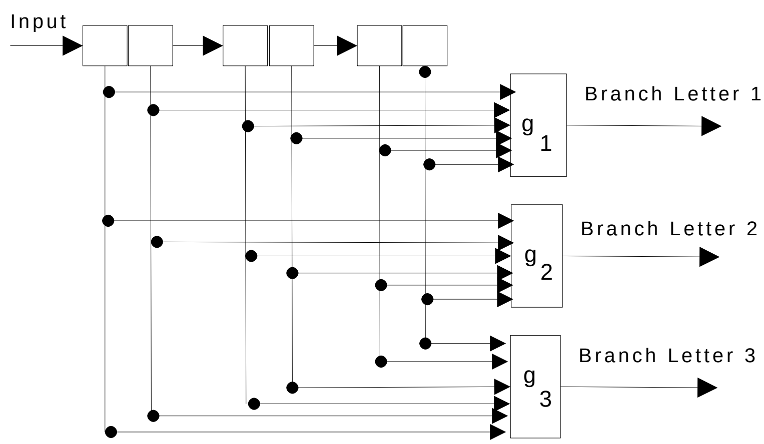

Figure 6.19: Finite-state machine realization of a rate $R = 2/3$ bits per source letter code.

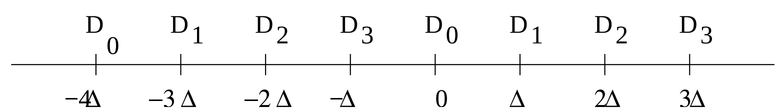

Figure 6.20: Partition of 8-level uniform quantizer levels into four cosets.

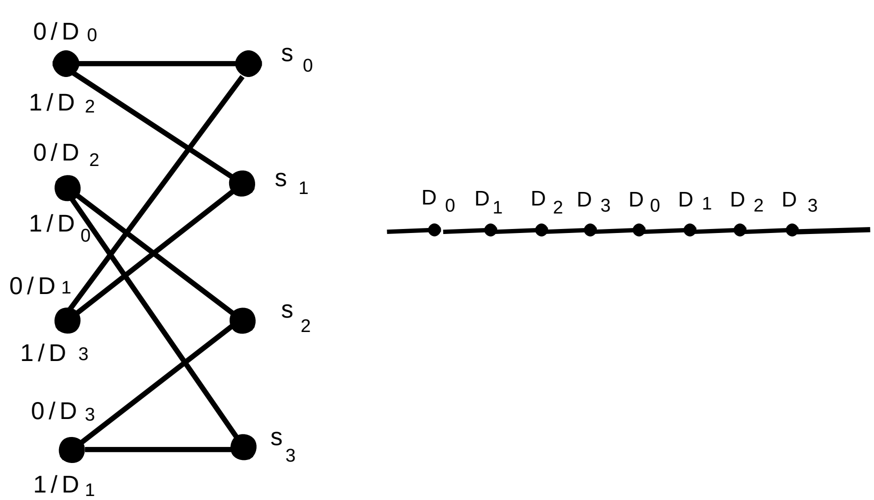

Figure 6.21: Trellis and cosets in TCQ.

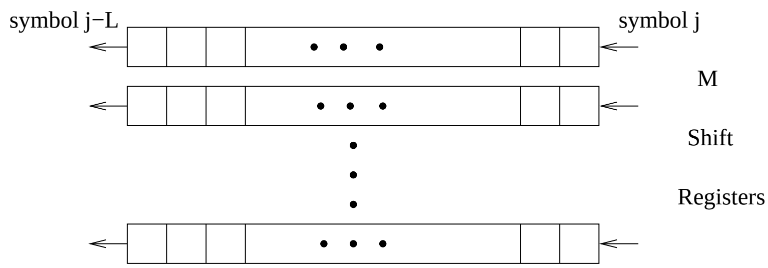

Figure 6.22: M shift registers of length L, each holding a path map symbol sequence. Symbol at time j shifted into every register from the right and left shift of each symbol in every register ejects symbol at time $j - L$ from its left end.

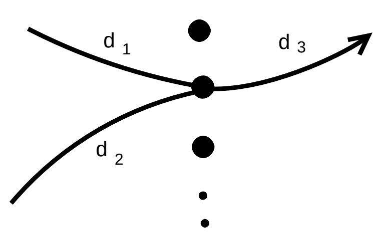

Figure 6.23: Paths through a trellis node.

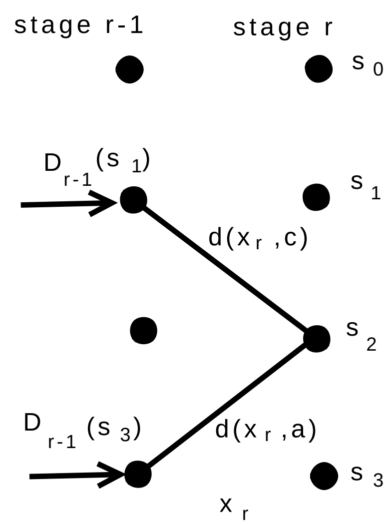

Figure 6.24: Distortions on paths converging to state s_2 at stage r in Viterbi Algorithm searching 4-state trellis of Fig. 6.17. Note that path symbol u_r must be 0 on both paths to converge to state s_2.

Chapter 7

Mathematical Transformations

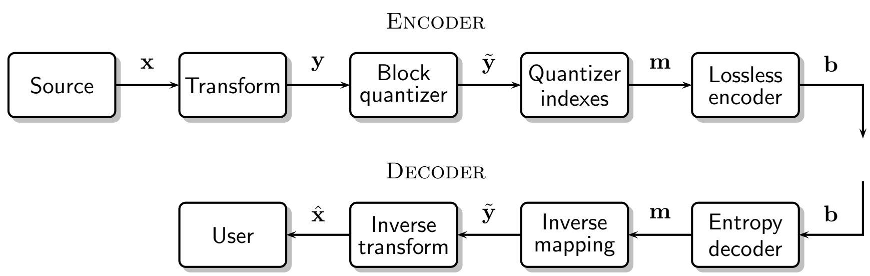

Figure 7.1: A transform coding system.

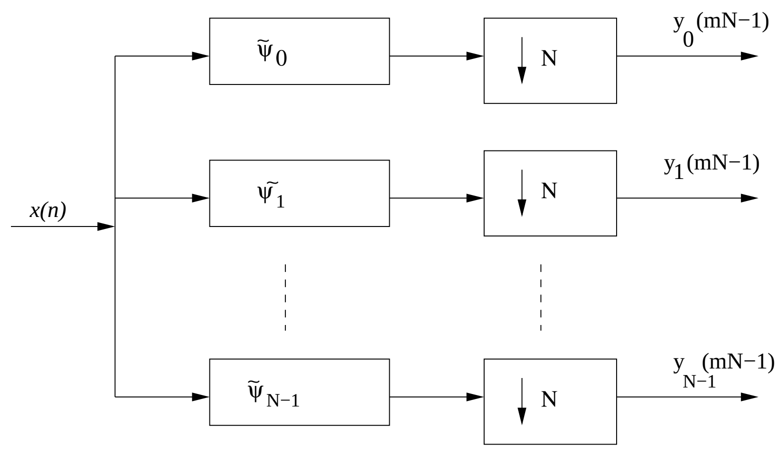

Figure 7.2: Forward N-point block transforms via a bank of N filters.

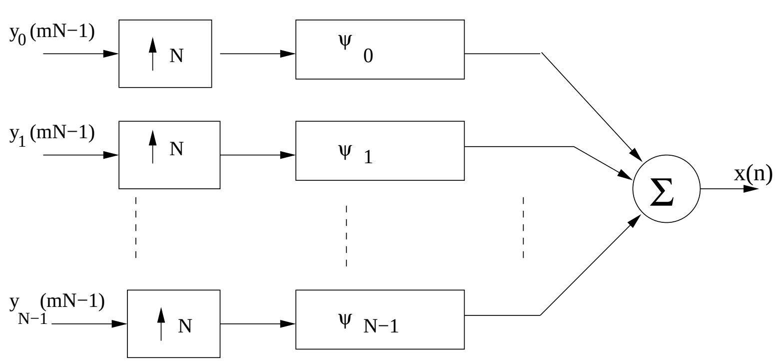

Figure 7.3: Inverse N-point block transforms via a bank of N filters.

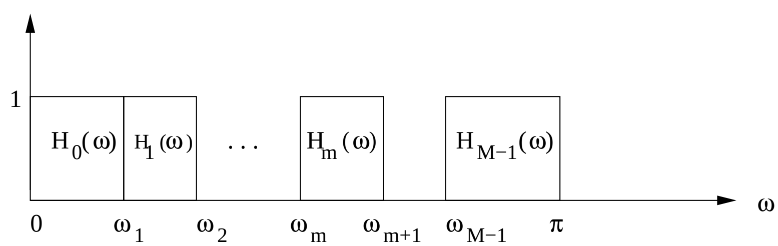

Figure 7.4: Subband filter transfer functions.

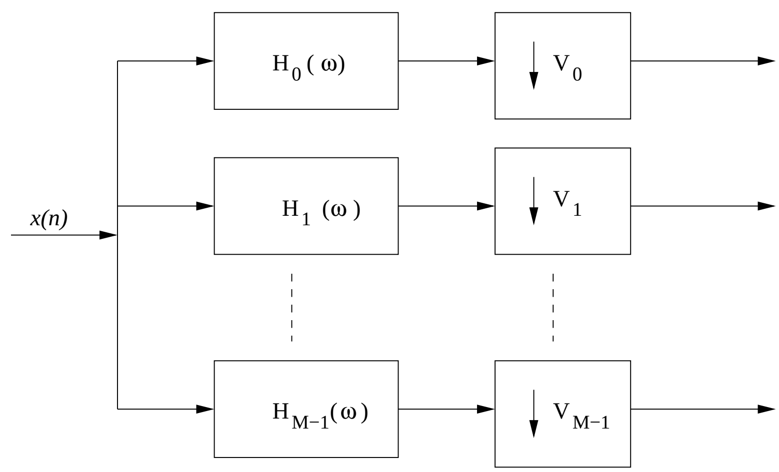

Figure 7.5: M-channel filter bank analysis of source into subbands.

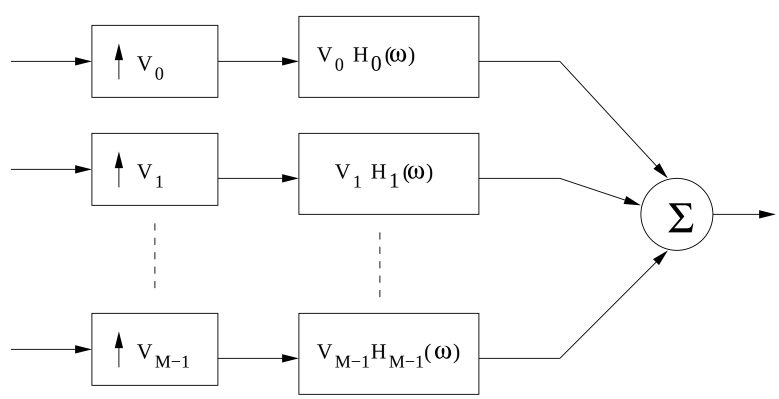

Figure 7.6: M-channel filter bank synthesis of source from subbands.

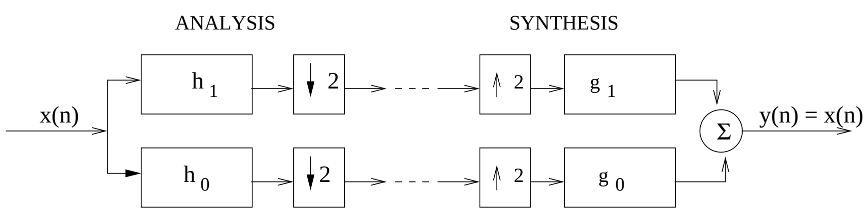

Figure 7.7: Two-channel analysis and synthesis filter banks. h_0 and g_0 denote impulse responses of the lowpass filters; h_1 and g_1 those of the highpass filters.

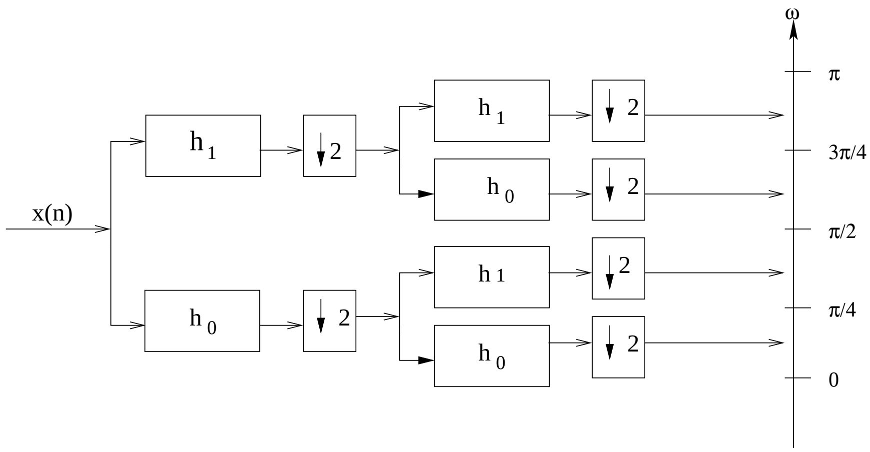

Figure 7.8: Two stages of two-channel analysis for four equal-size subbands.

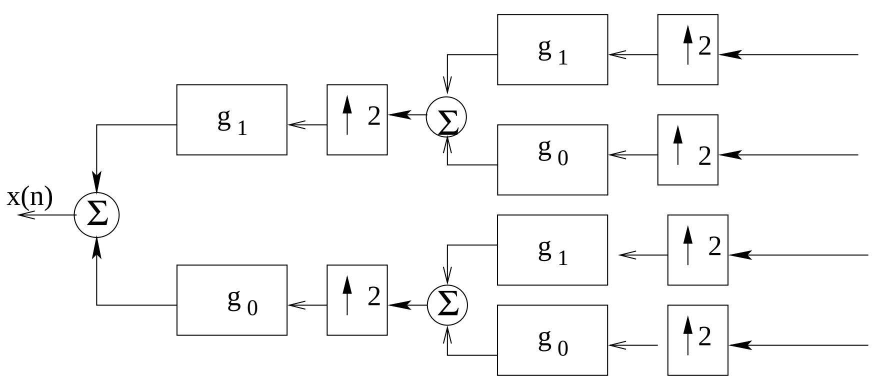

Figure 7.9: Two stages of two-channel synthesis to reconstruct signal from four subbands.

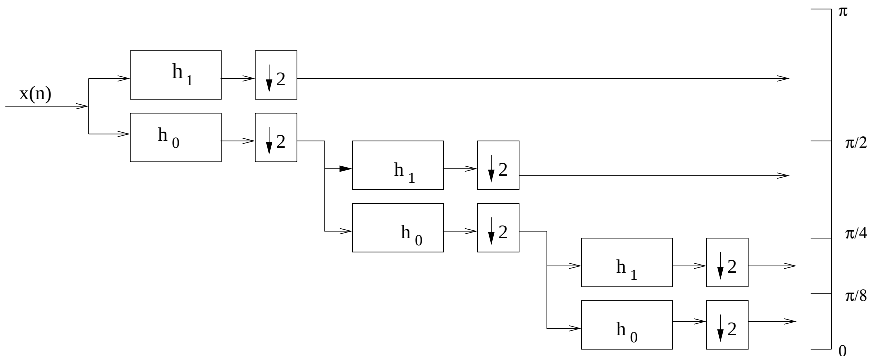

Figure 7.10: Three-level multiresolution anaysis.

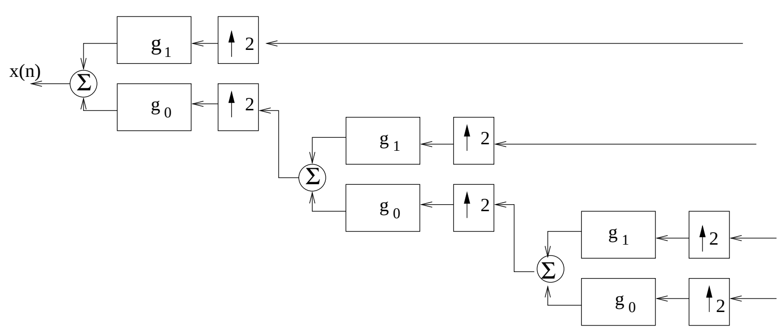

Figure 7.11: Three-level multiresolution synthesis.

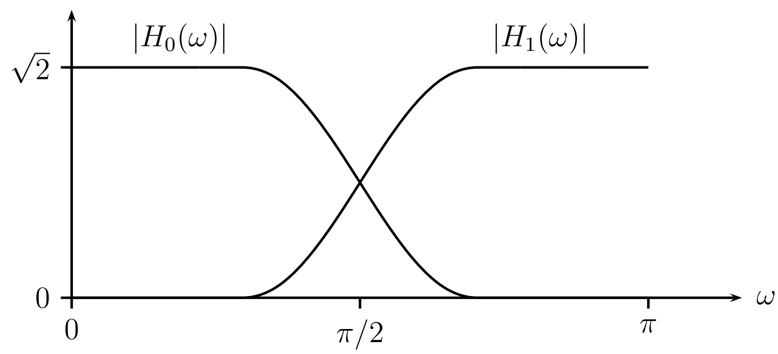

Figure 7.12: Alias-cancelling filters.

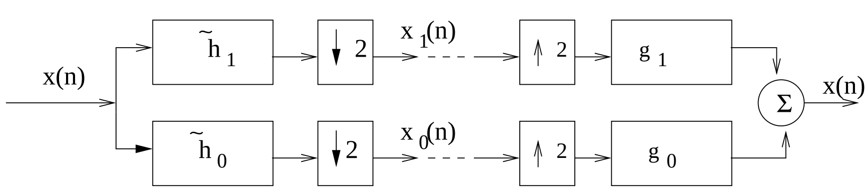

Figure 7.13: Two-channel analysis and synthesis biorthogonal filter banks. $\tilde{h}_0$ and g_0 denote impulse responses of the lowpass filters; $\tilde{h}_1$ and g_1 those of the highpass filters.

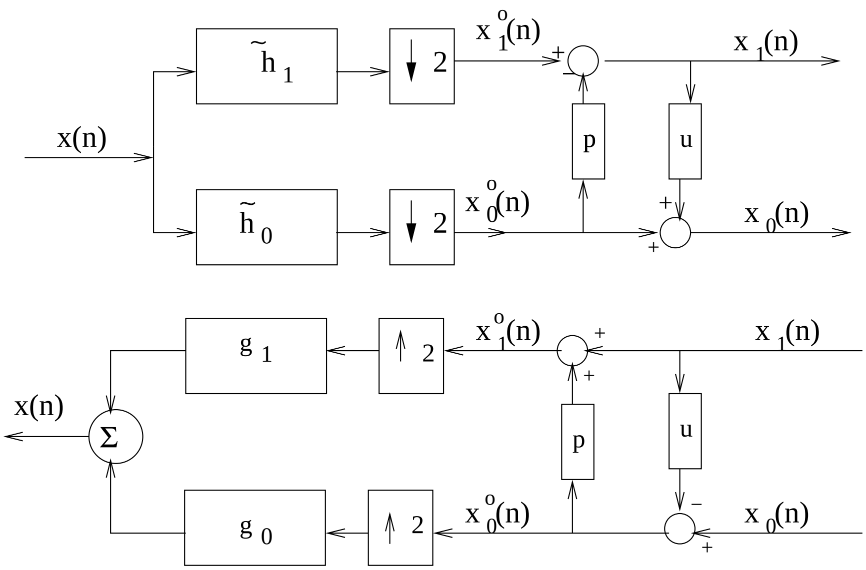

Figure 7.14: Analysis and synthesis stages of the lifting scheme.

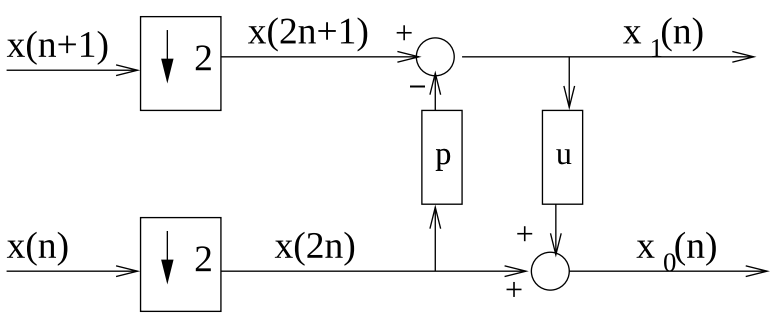

Figure 7.15: Analysis stage of the lifting scheme using the lazy wavelet transform.

Chapter 8

Rate Control in Transform Coding Systems

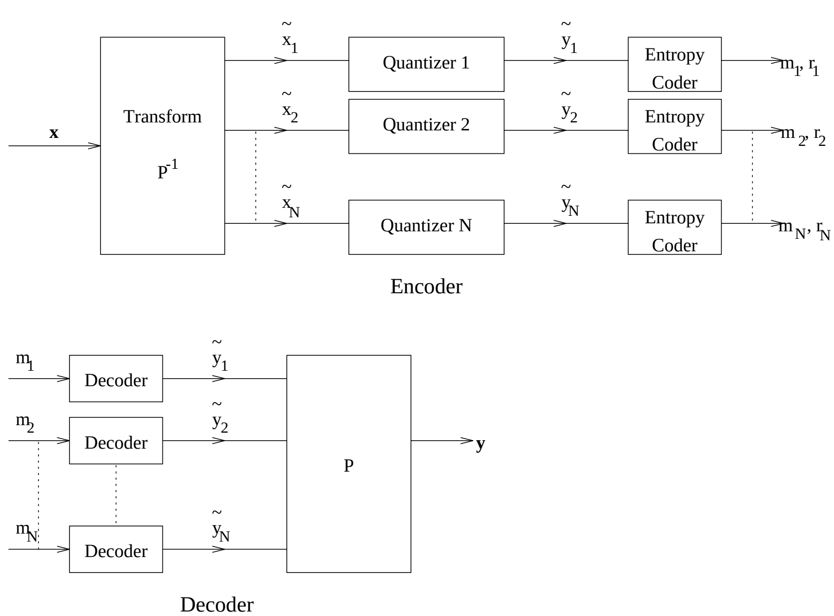

Figure 8.1: A transform coding system.

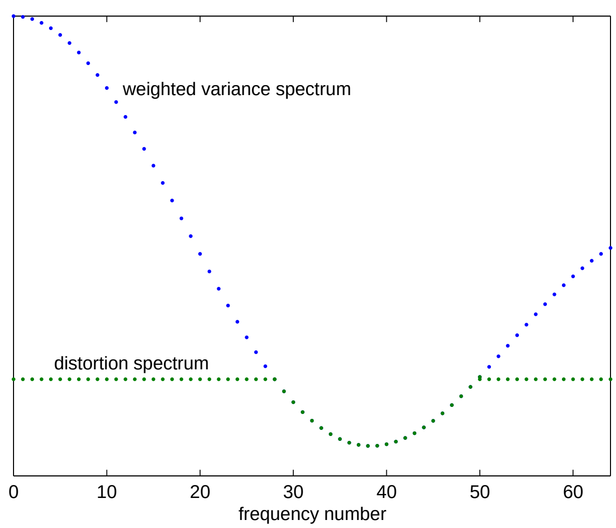

Figure 8.2: Weighted variance and distortion spectrum.

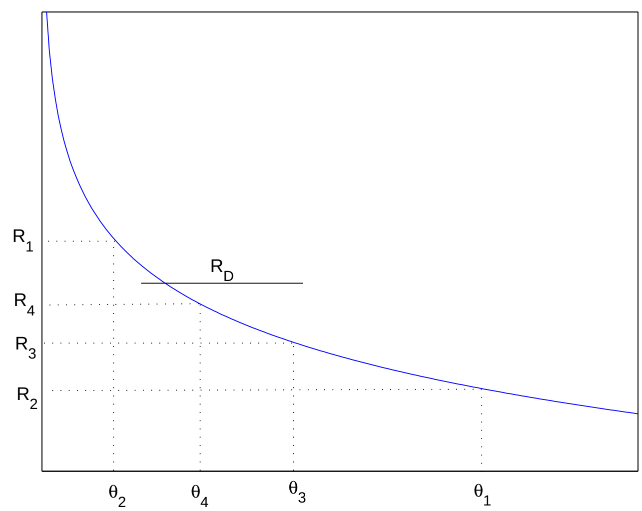

Figure 8.3: Illustration of initial points in bi-section procedure.

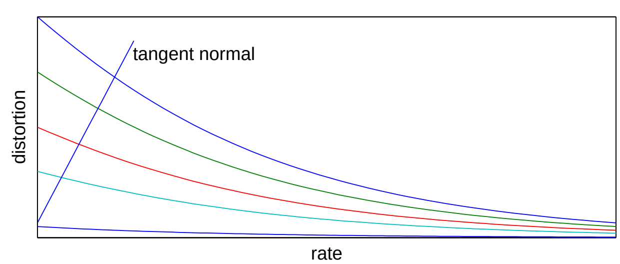

Figure 8.4: Illustration of equal slope condition on quantizers of different components.

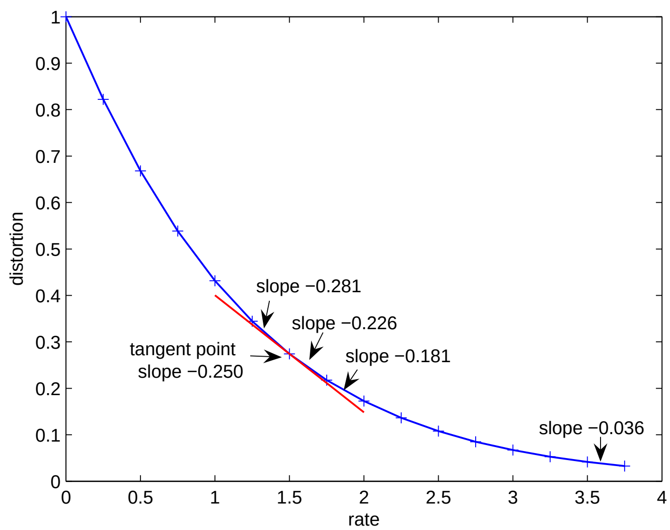

Figure 8.5: Seeking the desired slope by successive slope calculations starting from a high rate.

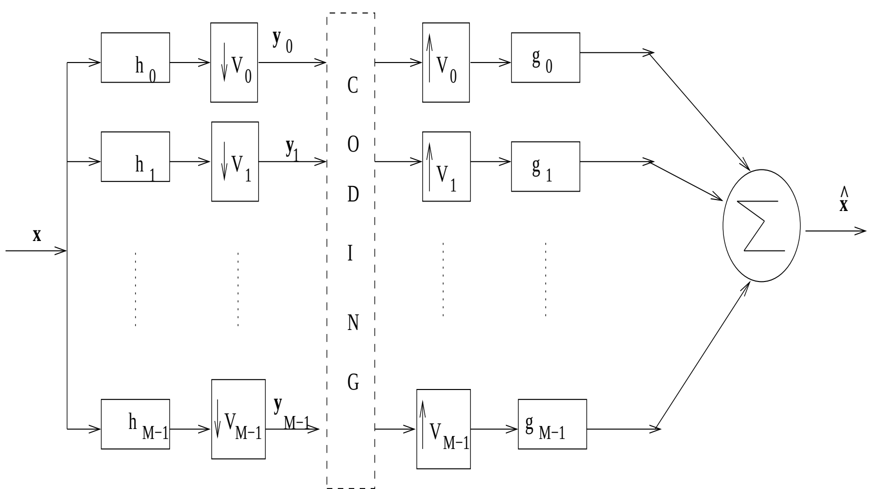

Figure 8.6: A subband analysis, coding, and synthesis system.

Chapter 9

Transform Coding Systems

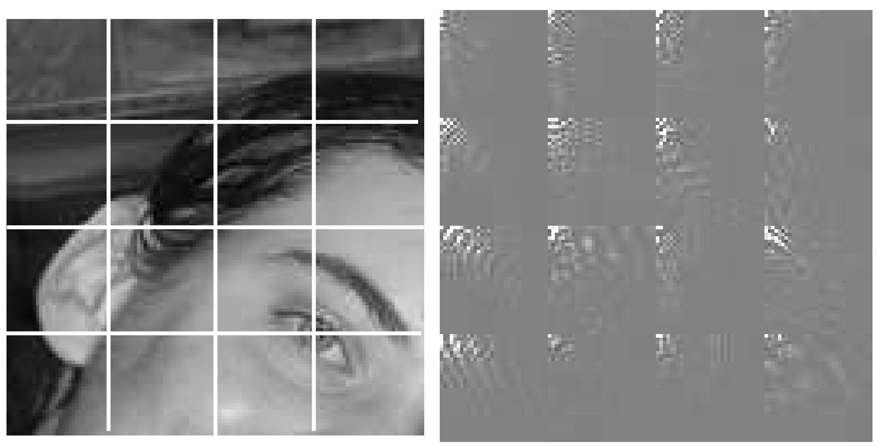

Figure 9.1: A 128×128 image divided into 32×32 blocks (left) and and a rendition of its blockwise DCT (right). For display purposes of the latter, the range of the transform was scaled and translated to the [0,255] interval with a middle gray value of 128.

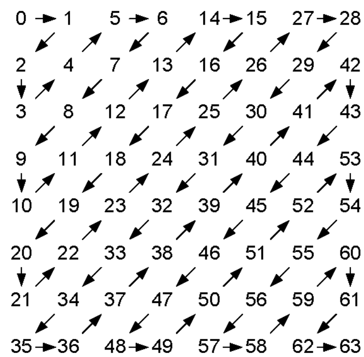

Figure 9.2: Zigzag scan of an image transform block.

0	1	4	5
2	3	6	7
8	9	12	13
10	11	14	15

Figure 9.3: Order of coding of 4×4 transform subblocks of a macroblock.

Chapter 10

Set Partition Coding

Figure 10.1: Lena image: dimension 512×512 pixels, 8 bits per sample.

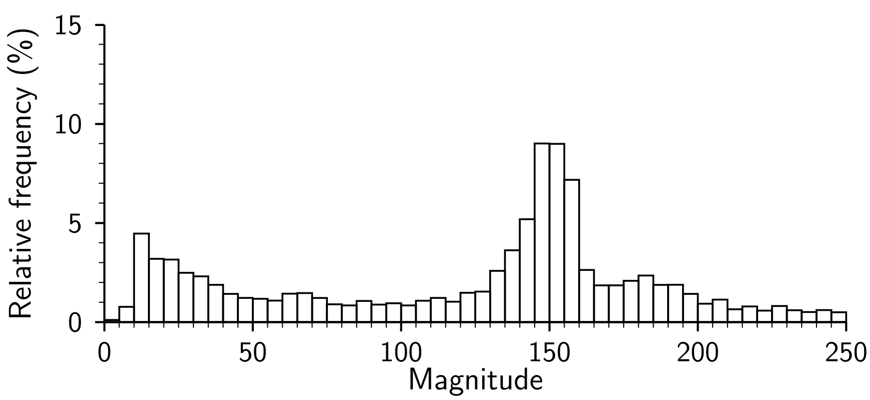

Figure 10.2: Distribution of pixel values for the Lena image.

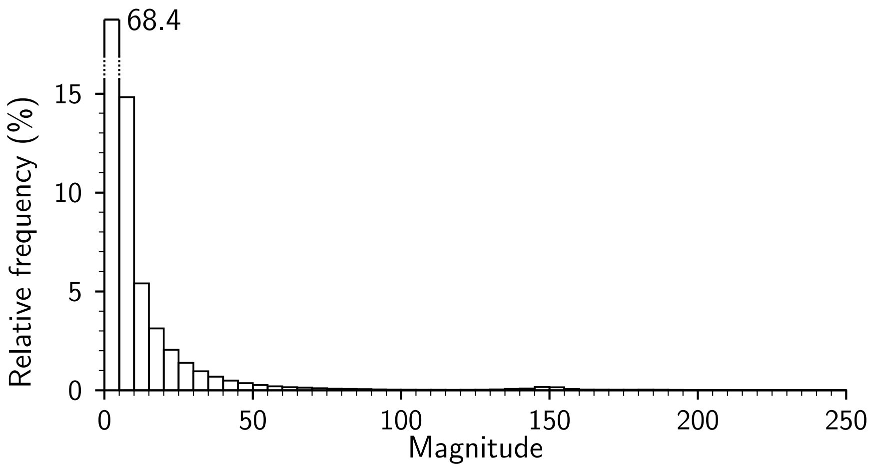

Figure 10.3: Distribution of magnitudes of integer transform coefficients of the Lena image.

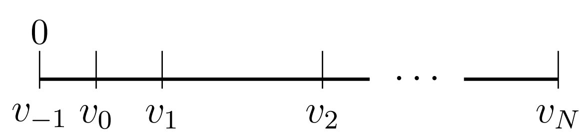

Figure 10.4: Set of thresholds marking ranges of values in dataset.

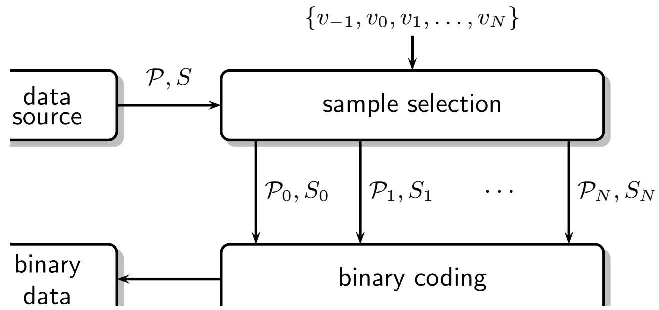

Figure 10.5: Separation of values in dataset before coding.

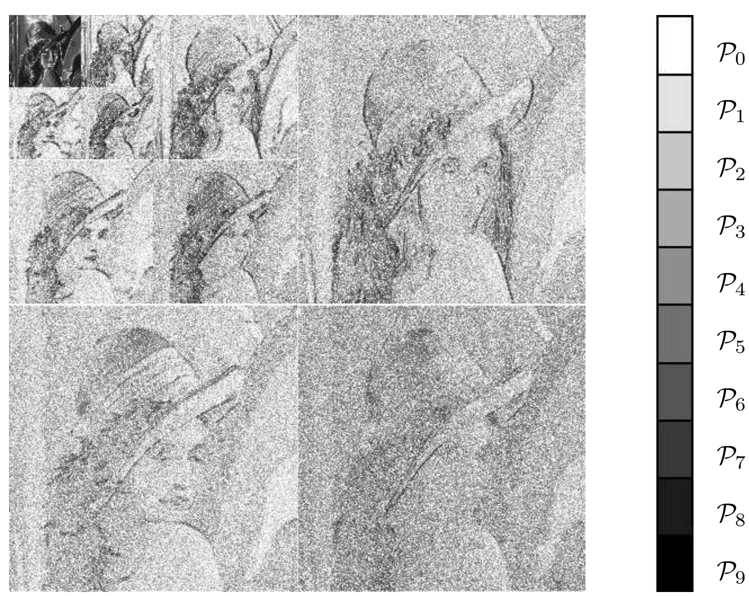

Figure 10.6: Distribution of magnitudes of integer-wavelet-transform coefficients. Logarithmic scale, darker pixels representing larger values. ($\mathcal{P}_n$ notation explained in Section 10.1.1.)

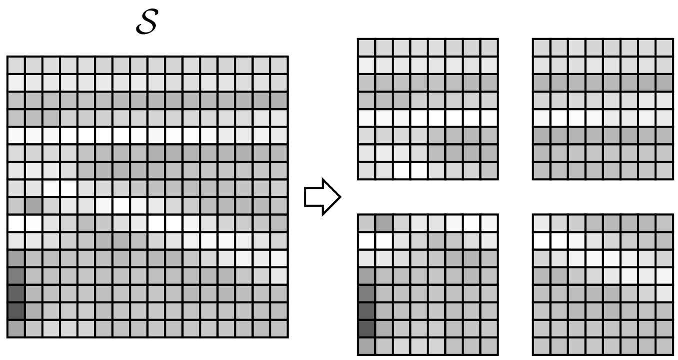

Figure 10.7: Partitioning of an array of pixels $\mathcal{S}$ into four equal-sized subsets. Gray values are used for representing pixel values.

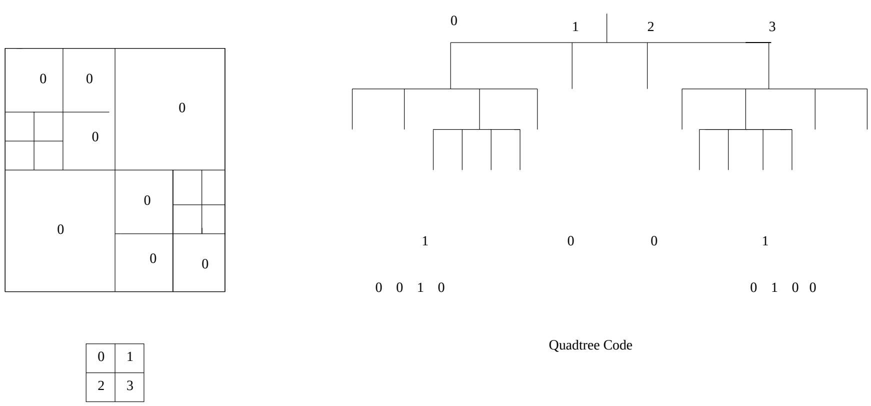

Figure 10.8: Three levels of quadrisection of 8x8 block and associated quadtree and code.

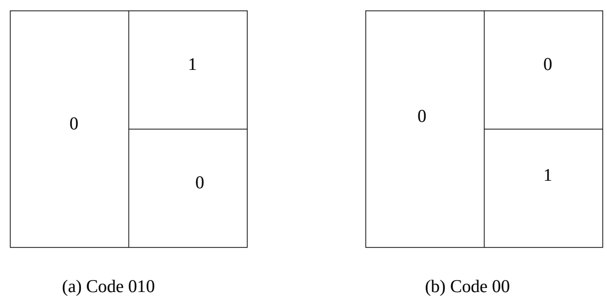

Figure 10.9: Bisection codes of significance patterns: (a) 0100 and (b) 0001.

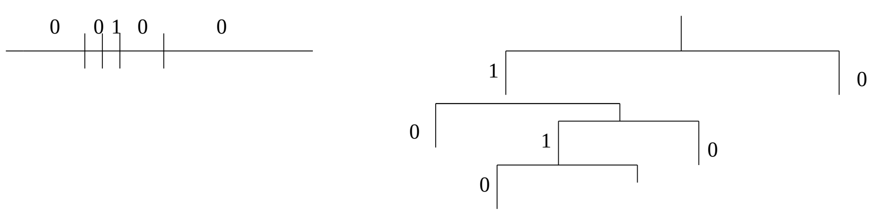

Figure 10.10: Bisection of signal– left, splitting pattern 10011001; right, corresponding binary tree (bintree) with bisection code 100100 labelled on branches.

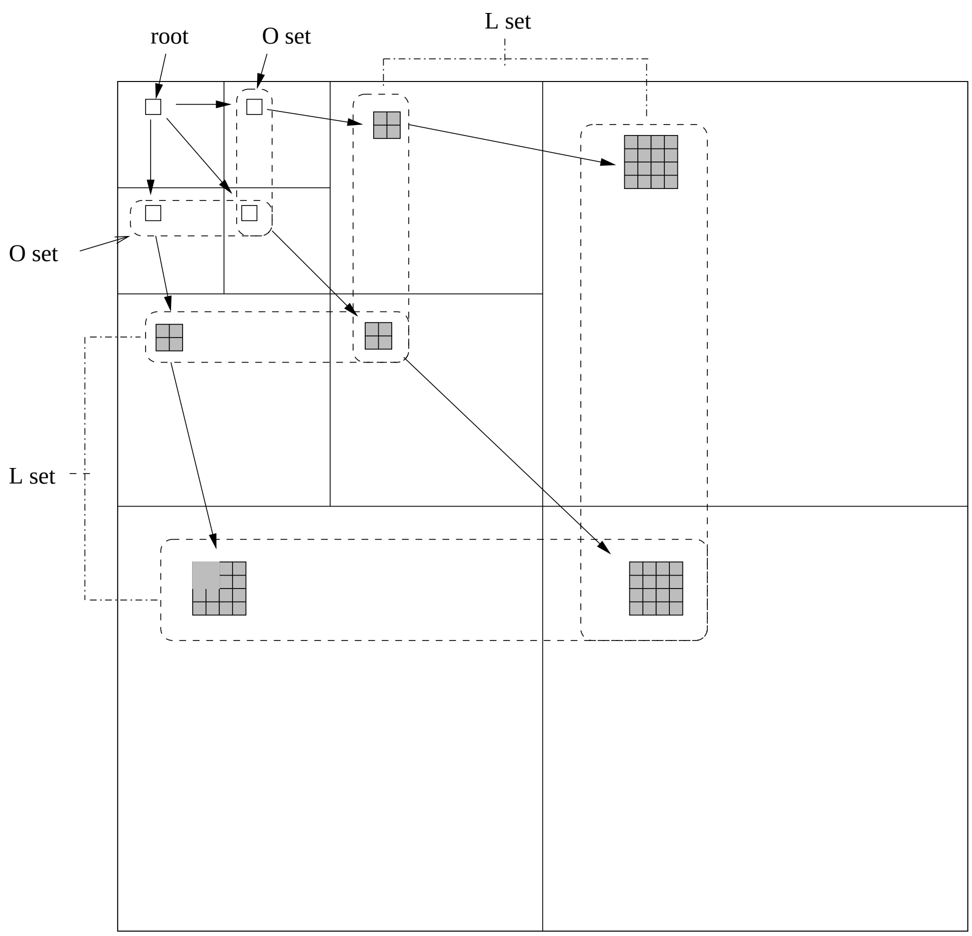

Figure 10.11: A spatial orientation tree (SOT) of a discrete wavelet transform. $\mathcal{O}$ denotes offspring set and $\mathcal{L}$ denotes grand-descendant set. The full descendant set $\mathcal{D} = \mathcal{O} \cup \mathcal{L}$.

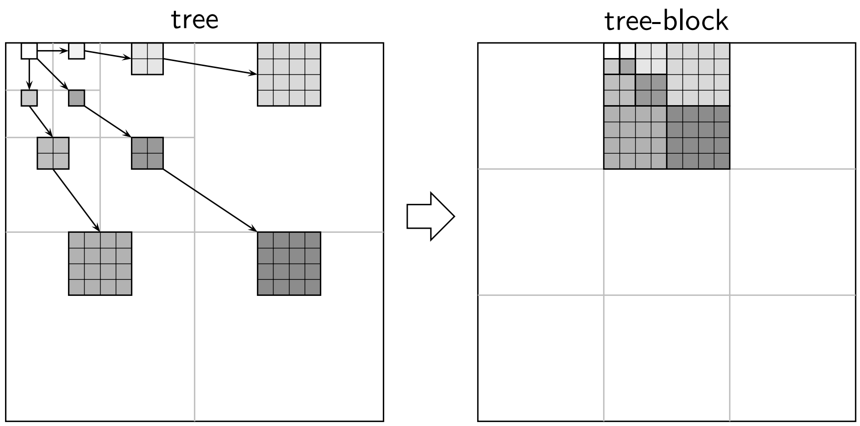

Figure 10.12: Rearranging a spatial orientation tree into a tree-block placed in the position of the image region it represents.

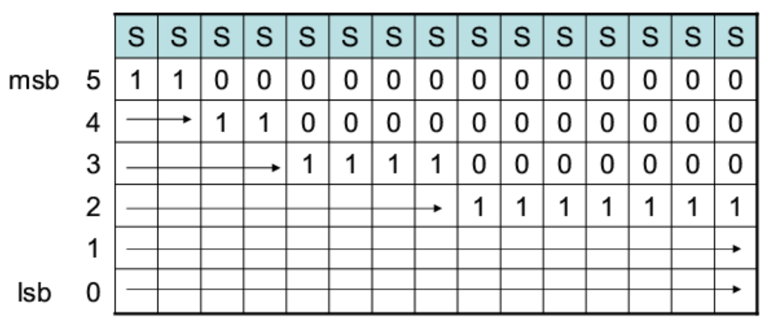

Figure 10.13: Progressive bit plane coding in the LIS for successive power of 2 thresholds. S above the most significant bit (msb) stands for the bit indicating the algebraic sign.

		S	S	S	S	S	S	S	S	S	S	S	S	S	S	S
msb	6	1	1	0	0	0	0	0	0	0	0	0	0	0	0	0
	5			1	1	0	0	0	0	0	0	0	0	0	0	0
	4					0	0	0	0	0	0	0	0	0	0	0
	3					1	1	1	0	0	0	0	0	0	0	0
	2								0	0	0	0	0	0	0	0
	1								1	1	1	0	0	0	0	0
lsb	0															

Figure 10.14: Progressive bit plane coding in the LIS for general thresholds. S above the most significant bit (msb) stands for the bit indicating the algebraic sign.

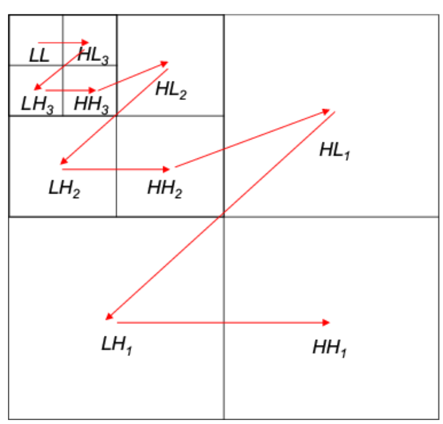

Figure 10.15: Scanning order of subbands in a 3-level wavelet decomposition. Subbands formed are named for horizontal and vertical low- or high-passband and level of decomposition, e.g., LH_2 is horizontal low passband and vertical high passband at second recursion level.

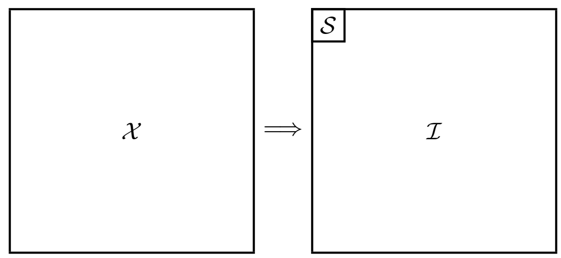

Figure 10.16: Partitioning of image $\mathcal{X}$ into sets $\mathcal{S}$ and $\mathcal{I}$.

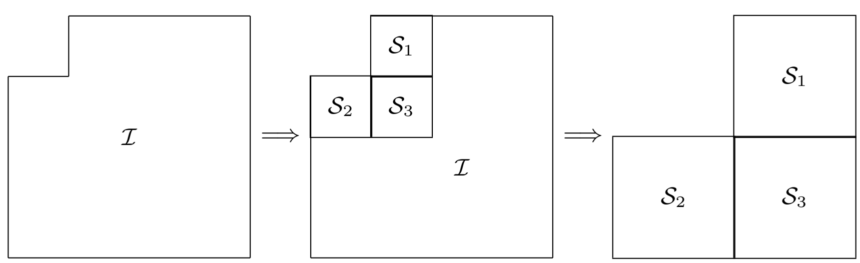

Figure 10.17: Partitioning of set $\mathcal{I}$.

	0	1	2	3	4	5	6	7
0	63	–34	49	10	7	13	–12	7
1	–31	23	14	–13	3	4	6	–1
2	15	14	3	–12	5	–7	3	9
3	–9	–7	–14	8	4	–2	3	2
4	–5	9	–1	47	4	6	–2	2
5	3	0	–3	2	3	–2	0	4
6	2	–3	6	–4	3	6	3	6
7	5	11	5	6	0	3	–4	4

Figure 10.18: Example of coefficients in an 8×8 transform used by example. The numbers outside the box are vertical and horizontal coordinates.

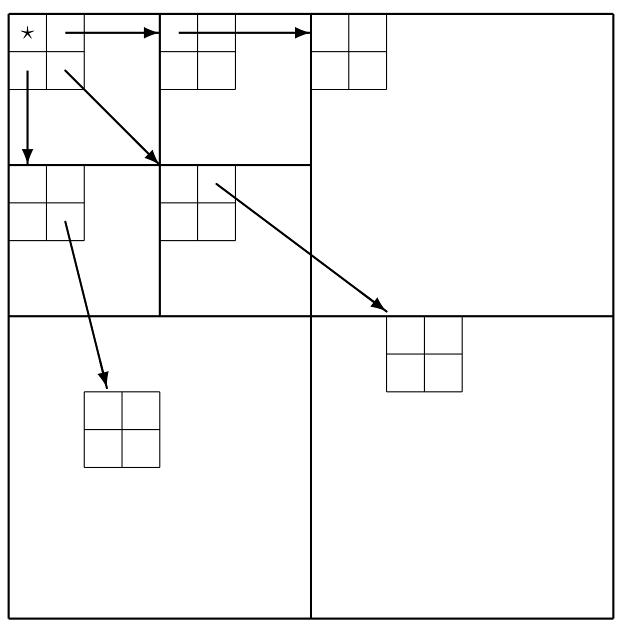

Figure 10.19: Examples of parent-offspring dependencies in the spatial-orientation trees. Coefficients in the LL band marked "*" have no descendants.

Chapter 11

Subband/Wavelet Coding Systems

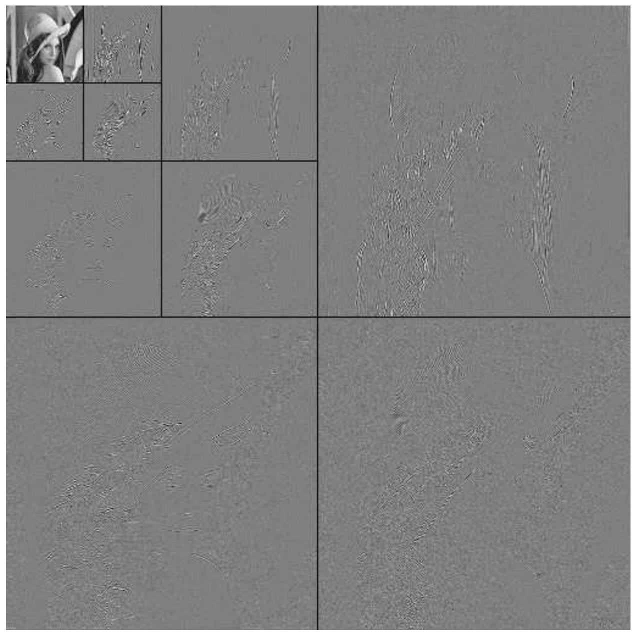

Figure 11.1: Display of image subbands of a 3-level, dyadic wavelet transform. Middle grey level of 128 corresponds to 0 value of a coefficient in all subbands, excluding the lowest frequency one in the top left corner.

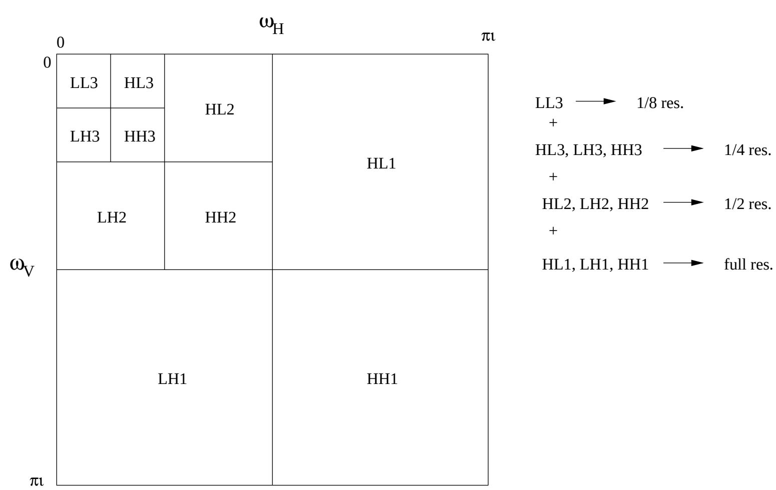

Figure 11.2: Subbands of a 3-level, dyadic wavelet transform.

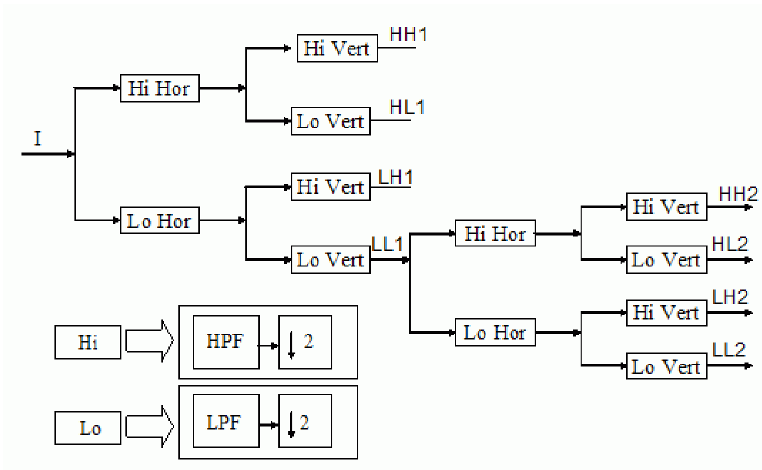

Figure 11.3: Two-level recursive lowpass filter analysis of image I.

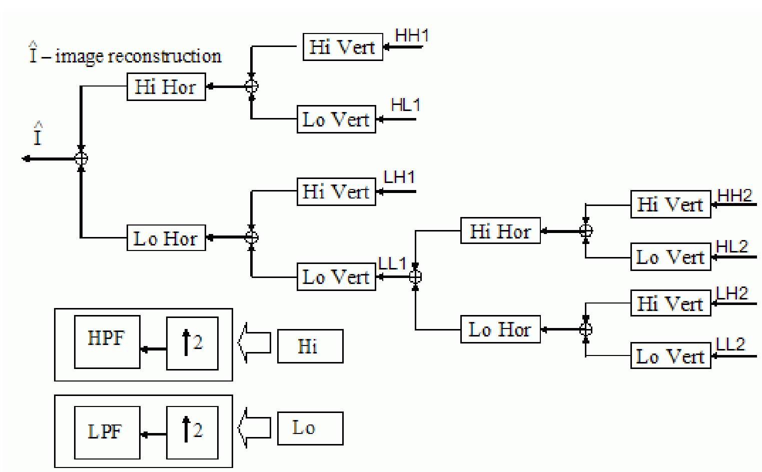

Figure 11.4: Two-level recursive lowpass filter synthesis of image $\hat{I}$.

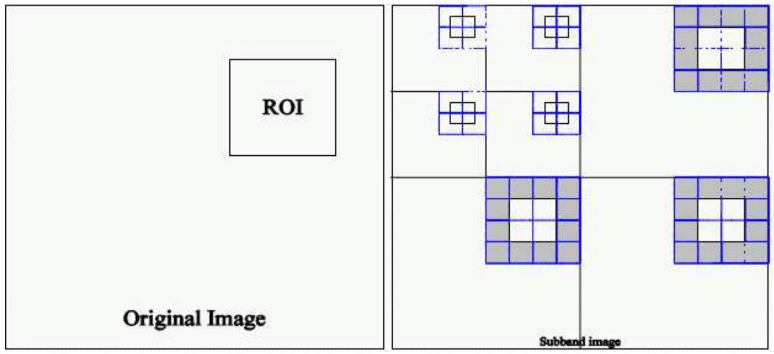

Figure 11.5: Subband regions in the wavelet transform corresponding to an image region. The inner rectangles correspond to the exact corresponding fractional area of the image region of interest (ROI). The areas between the inner and outer rectangles contain coefficients needed to reconstruct ROI exactly.

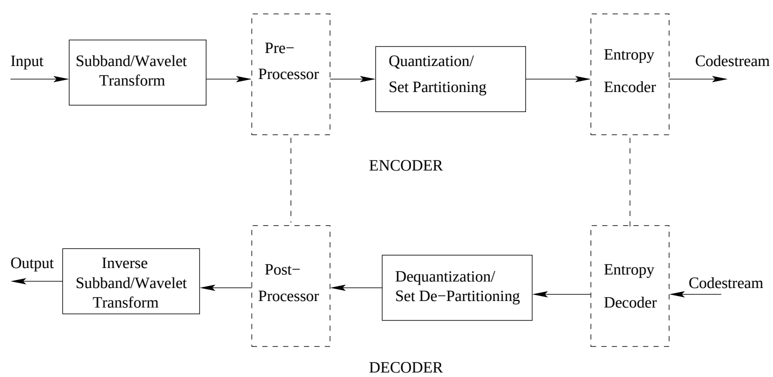

Figure 11.6: Encoder and decoder of subband/wavelet transform coding system. The boxes with dashed lines denote optional actions.

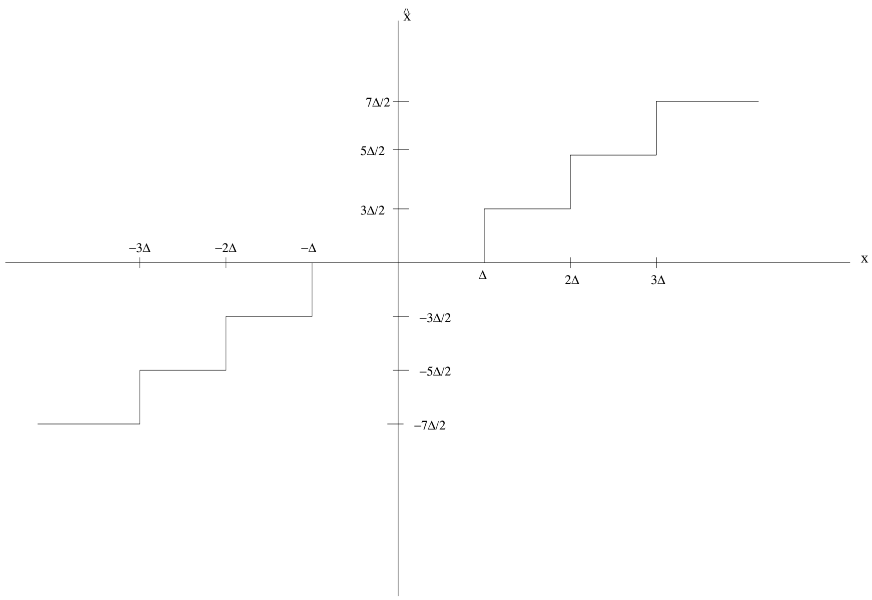

Figure 11.7: Input-output characteristic of a 7 level, uniform null-zone quantizer.

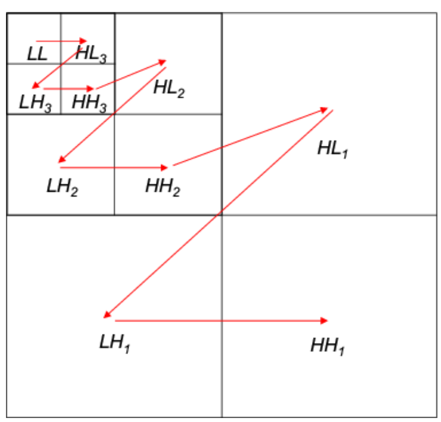

Figure 11.8: Scanning order of subbands in a 3-level wavelet decomposition. Subbands formed are named for horizontal and vertical low- or high-passband and level of decomposition, e.g., LH_2 is horizontal low passband and vertical high passband at second recursion level.

Figure 11.9: Original 512×512, 8 bits/pixel Goldhill image.

Figure 11.10: Reconstructions from codestream of Goldhill coded to rate 1.329 bpp, quantizer step size = 1/0.31 at full, 1/2, and 1/4 resolutions.

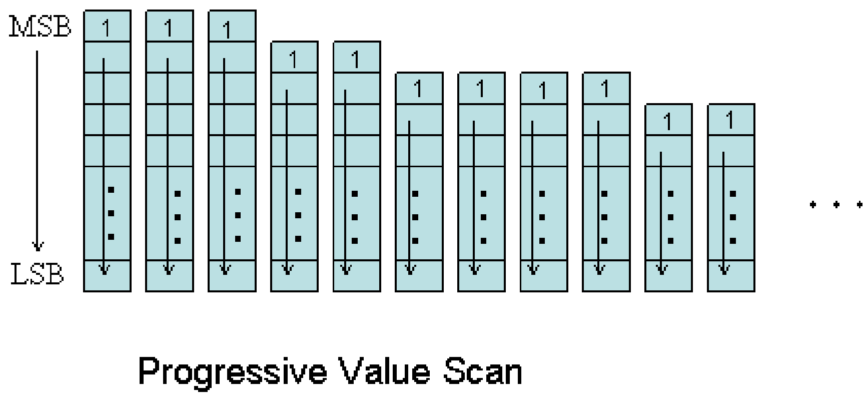

Figure 11.11: Coding order for a progressive value codestream.

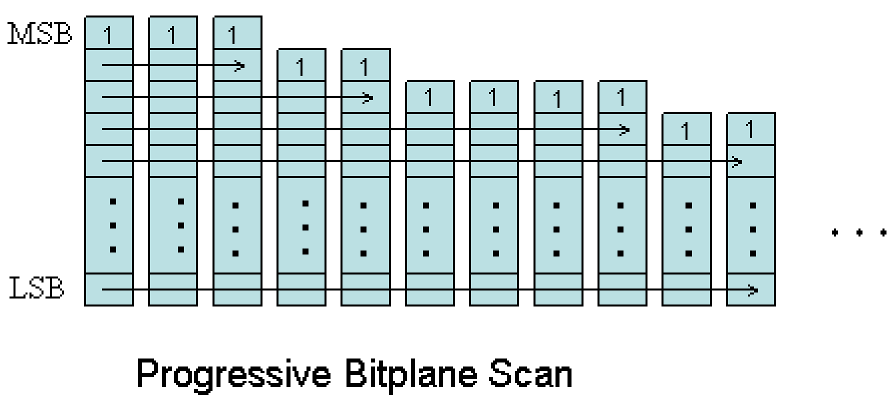

Figure 11.12: Coding order for a bit embedded codestream.

Figure 11.13: Reconstructions of Goldhill from same codestream by a quality scalable coding method.

(a) 2.00 bpp, 42.02 dB	(b) 1.00 bpp, 36.55 dB
(c) 0.50 bpp, 33.13 dB	(d) 0.25 bpp, 30.56 dB

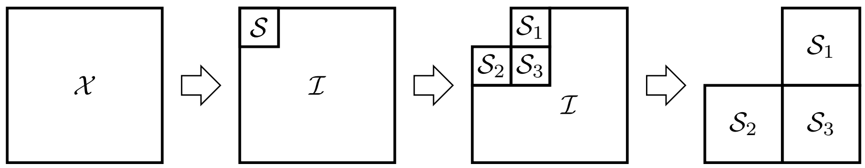

Figure 11.14: Partitioning of image $\mathcal{X}$ into sets $\mathcal{S}$ and $\mathcal{I}$, and subsequent partitioning of set $\mathcal{I}$.

Figure 11.15: Uncoded (left) and coded (right) reconstructions of 512×512 lena image with identical quantizer step sizes. Both have PSNR=37.07 dB; rate of uncoded (left) = 0.531 bpp and rate of coded (right) is 0.500 bpp.

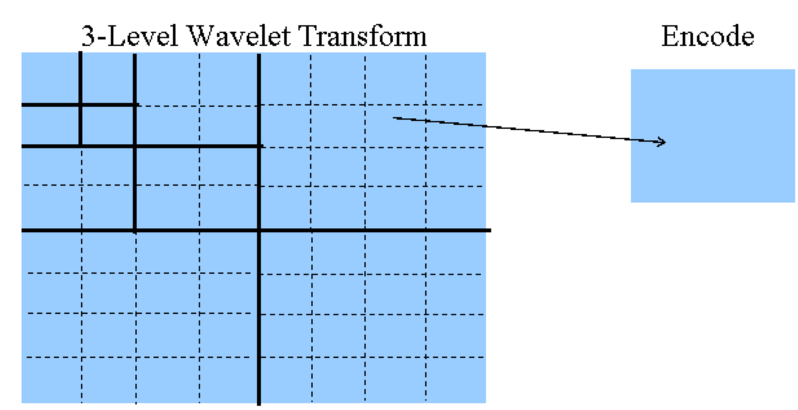

Figure 11.16: Division of wavelet subbands into subblocks. Note subbands of coarsest level are too small to be divided.

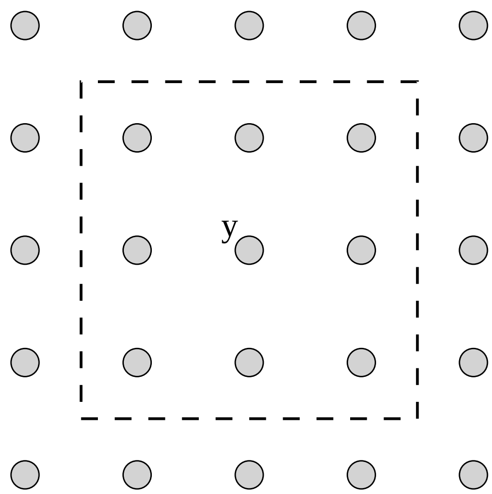

Figure 11.17: Eight pixel neighborhood of pixel y for context formation.

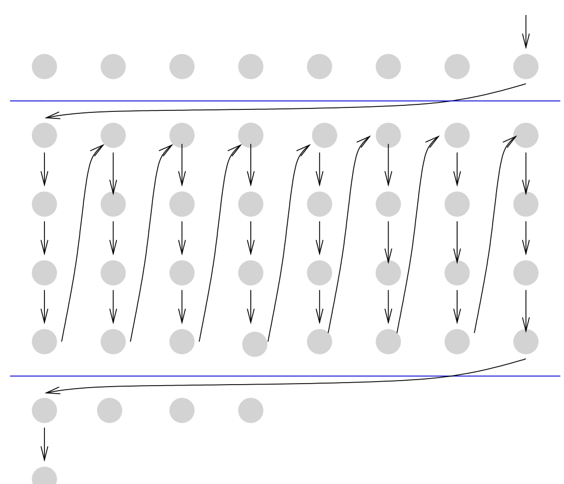
Figure 11.18: Column-wise scan pattern of stripes within a code-block.

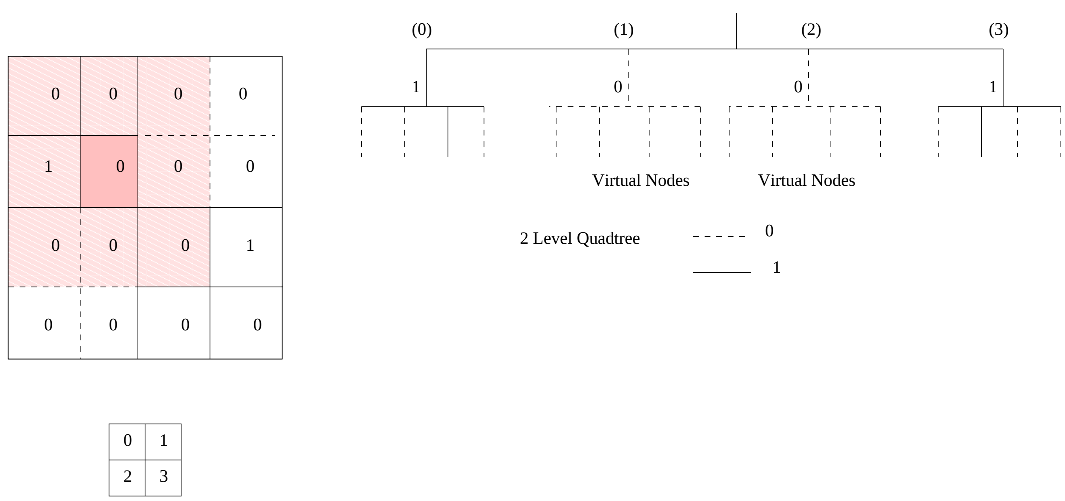

Figure 11.19: Two levels of quadrisection of 8x8 block and associated quadtree, including virtual nodes.

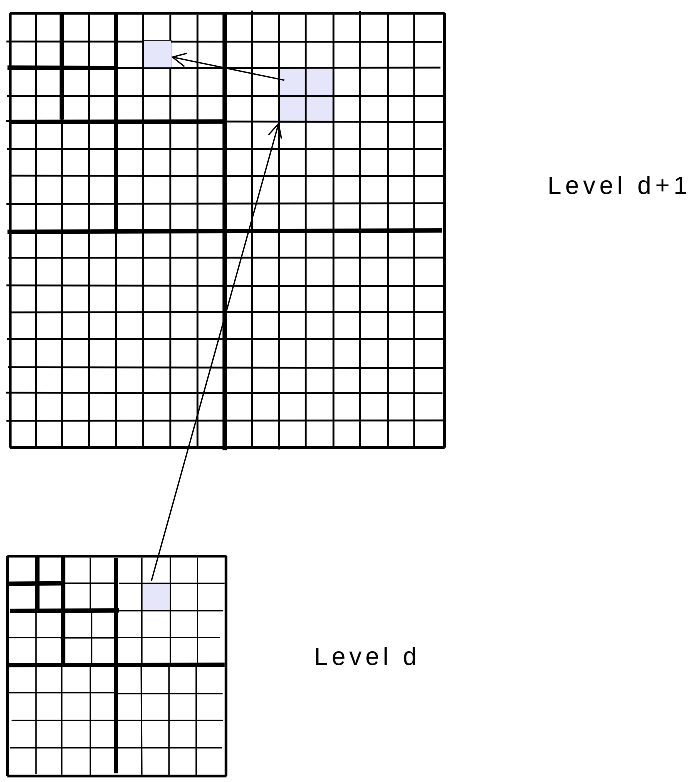

Figure 11.20: Two successive levels of quadtree with nodes located in wavelet transform and dependency relationships.

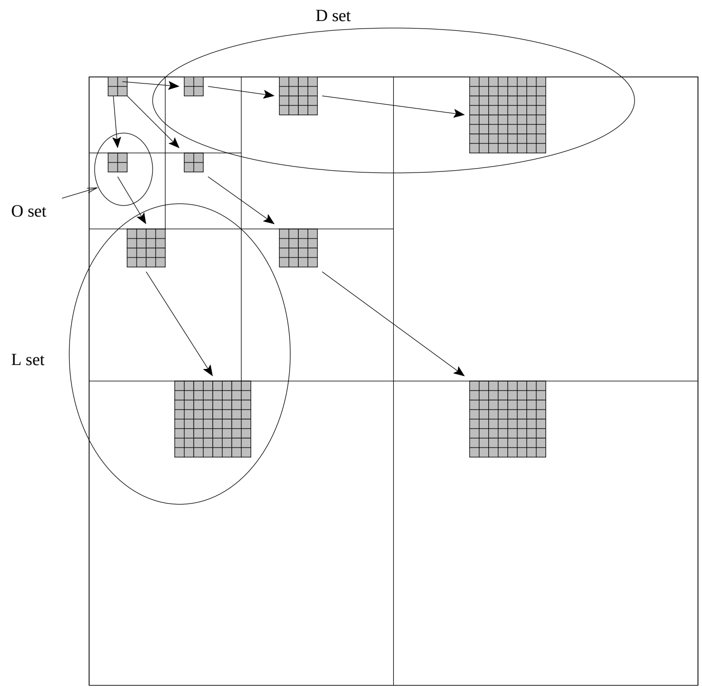

Figure 11.21: Illustration of set types in a tree-block with its three constituent SOT's descending from a 2×2 group in the lowest frequency subband in a three level, 2D wavelet transform. A full descendant $\mathcal{D}$ set, an offspring $\mathcal{O}$ set, and a grand-descendant $\mathcal{L}$ set are encircled in the diagram. All pixels (coefficients) in grey, including the upper left corner pixel in the 2×2 group, belong to the tree-block.

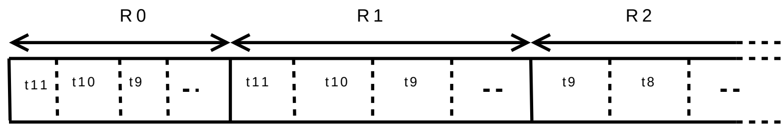

Figure 11.22: Resolution scalable bitstream structure. $\mathcal{R}_0, \mathcal{R}_1, \ldots$ denote the segments with different resolutions, and $t_{11}, t_{10}, \ldots$ the different thresholds ($t_n = 2^n$.) Note that in $\mathcal{R}_2$, t_{11} and t_{10} are empty.

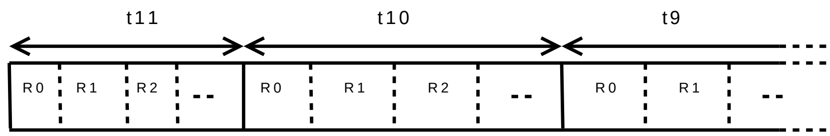

Figure 11.23: Quality scalable bitstream structure. $\mathcal{R}_0, \mathcal{R}_1, \ldots$ denote the segments of different resolutions, and $t_{11}, t_{10}, \ldots$ the different thresholds ($t_n = 2^n$). At higher thresholds, some of the finer resolutions may be empty.

Figure 11.24: Reconstructions from same codestream of 512×512 Goldhill, quantizer step size $= 1/0.31$, coded to rate 1.329 bpp, and of 70×128 region at coordinates (343,239).

Chapter 12

Methods for Lossless Compression of Images

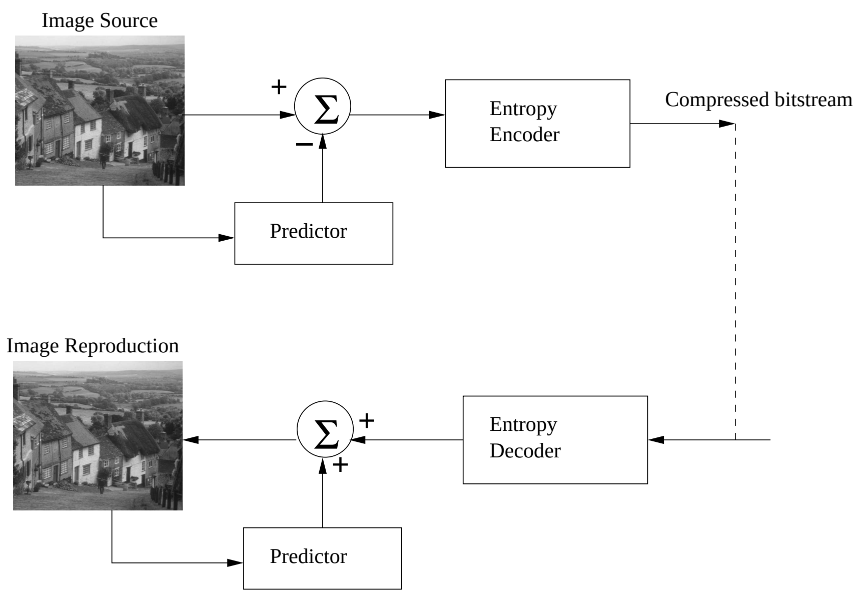

Figure 12.1: Lossless predictive coding and decoding of image sources.

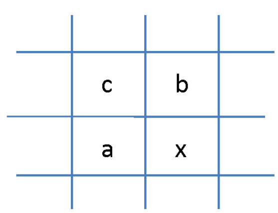

Predictor No.	Prediction
0	none
1	a
2	b
3	c
4	a+b-c
5	a+(b-c)/2
6	b+(a-c)/2
7	(a+b)/2

Figure 12.2: Neighborhood and prediction modes for lossless JPEG.

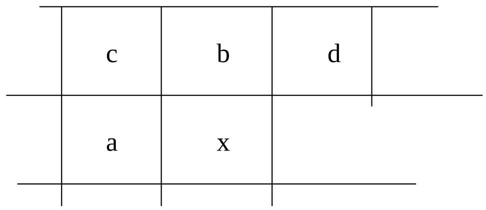

$$\hat{x} = \begin{cases} \min(a,b), & \text{if } c \geq \max(a,b) \\ \max(a,b), & \text{if } c \leq \min(a,b) \\ a+b-c, & \text{otherwise} \end{cases}$$

Figure 12.3: Causal template and predictor for JPEG-LS.

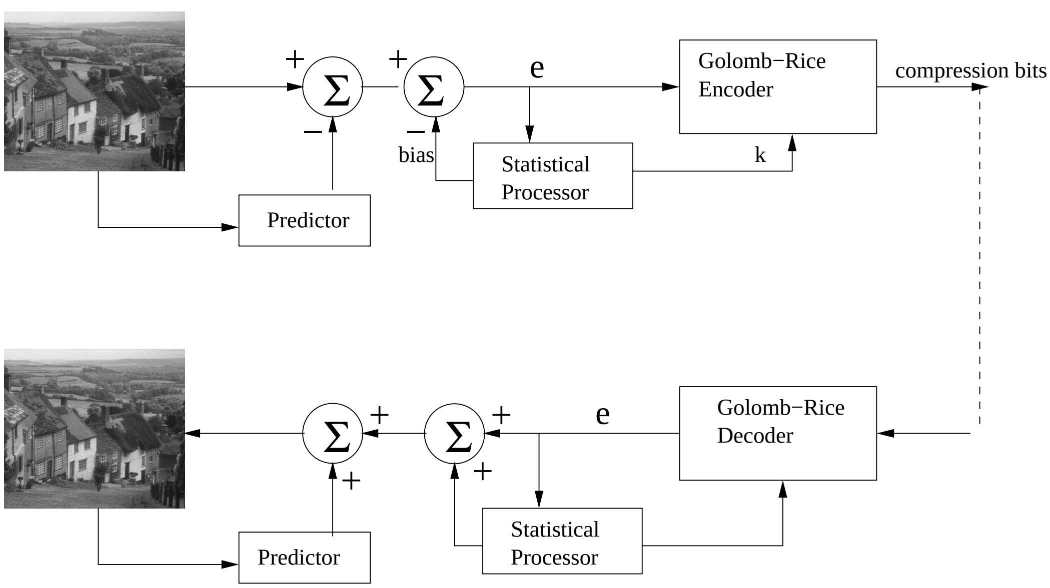

Figure 12.4: Coding and decoding system in JPEG-LS.

Chapter 13

Color and Multi-Component Image and Video Coding

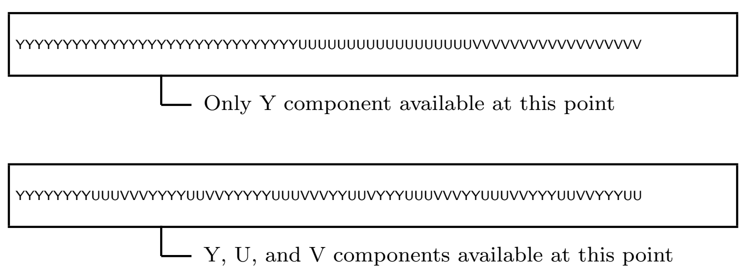

Figure 13.1: Compressed color bitstreams: conventional (top) and embedded (bottom).

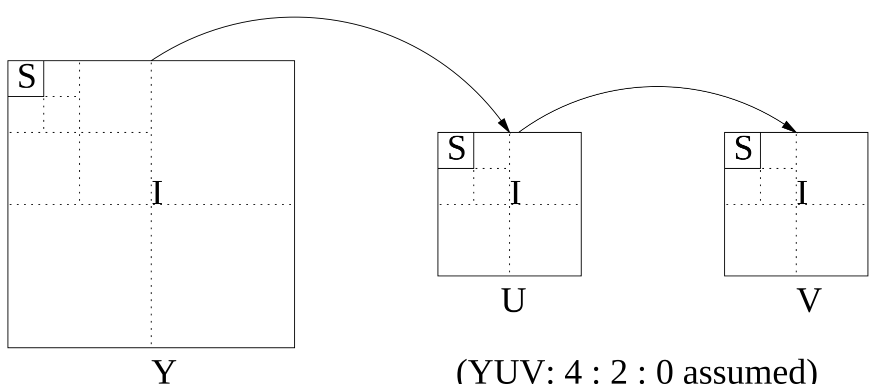

Figure 13.2: Set partitioning and color plane traversal for CSPECK. Coding proceeds in order of Y, U, and V at the same significance threshold.

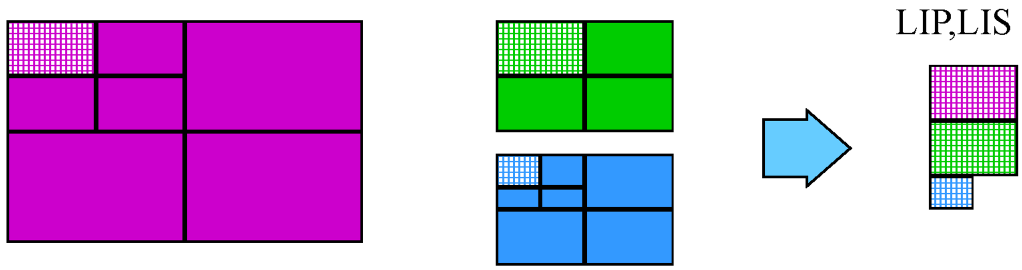

Figure 13.3: Initial control lists of color SPIHT for the Y, U and V transform planes in 4:2:0 subsampling format.

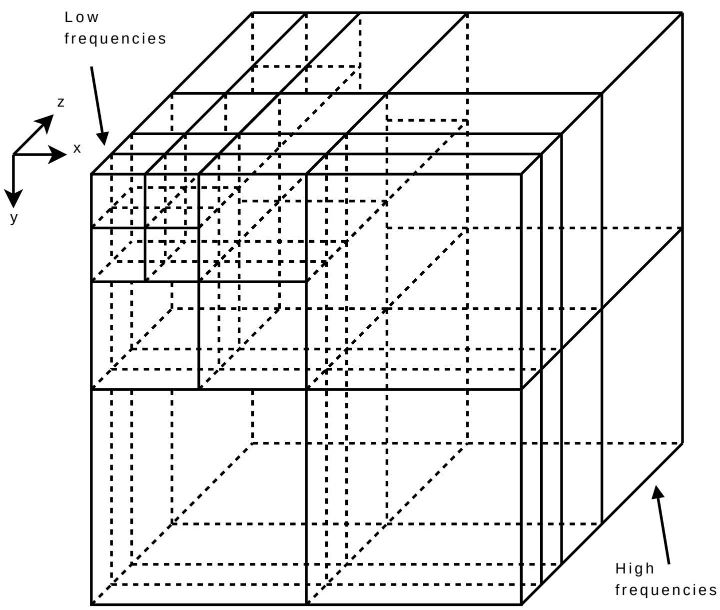

Figure 13.4: Subbands of a wavelet packet transform with three spatial levels and two axial levels.

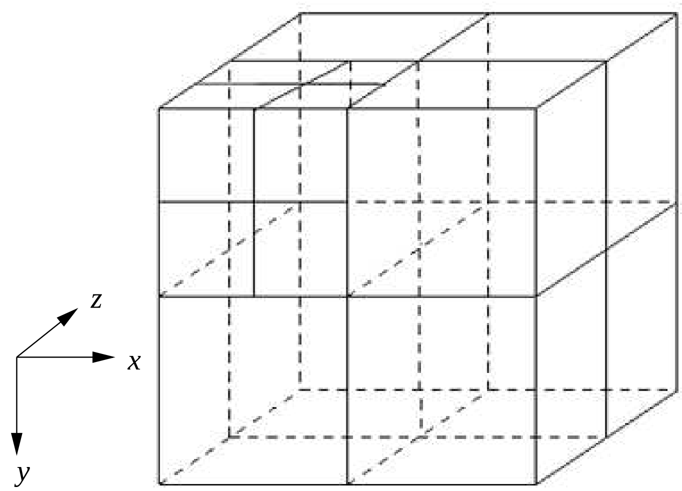

Figure 13.5: Subbands of a dyadic wavelet transform with alternating decomposition to two levels in the three directions.

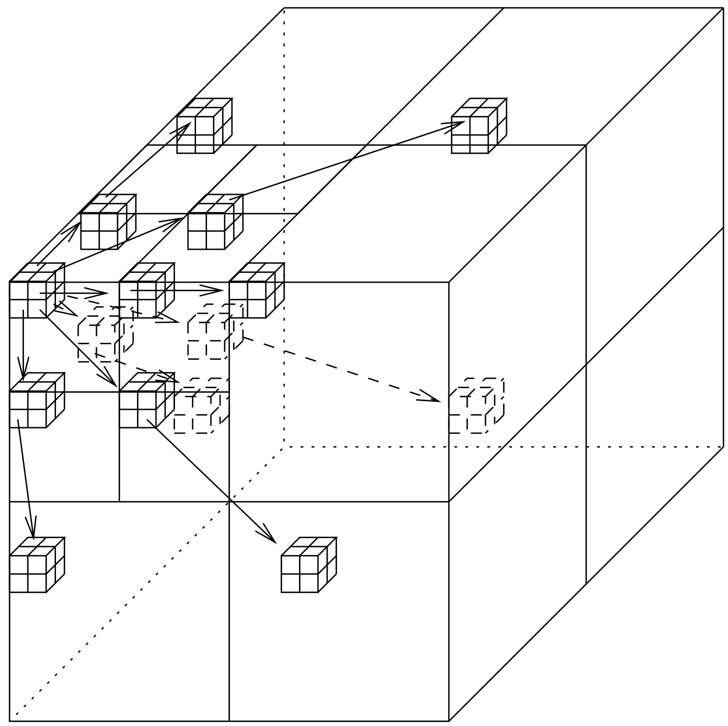

Figure 13.6: Symmetric 3-D tree structure for SPIHT coding.

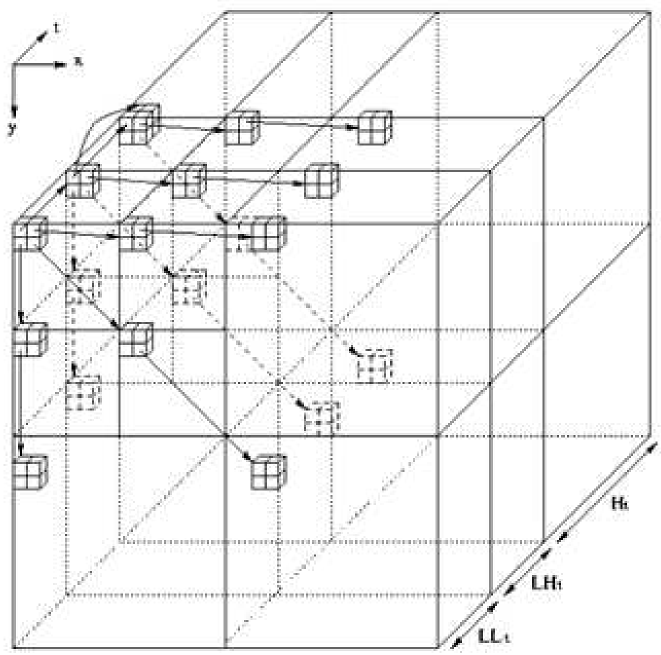

Figure 13.7: Asymmetric 3-D tree structure for SPIHT coding.

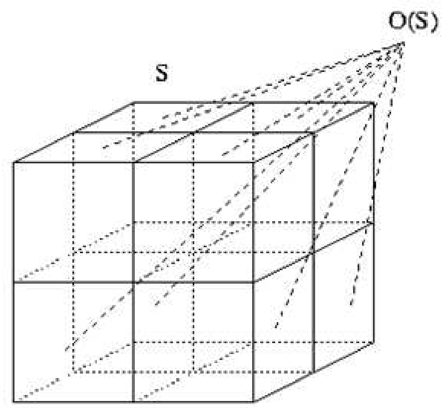

Figure 13.8: Splitting a significant block S into its eight offspring blocks $O(S)$.

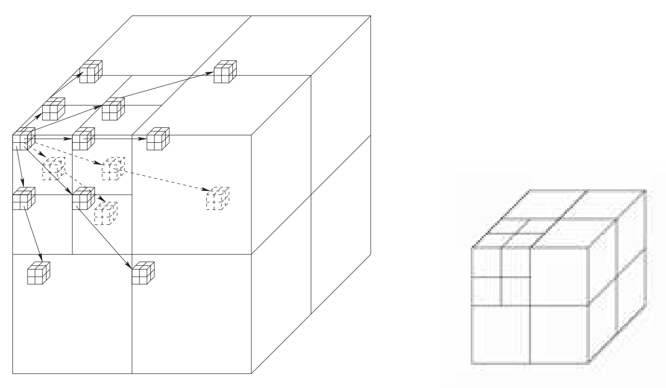

Figure 13.9: The block tree (right) of a $2 \times 2 \times 2$ root group in the lowest frequency subband (left, top left corner).

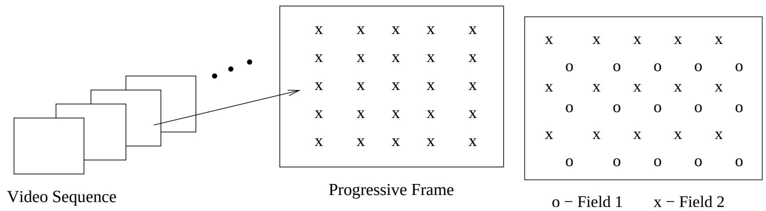

Figure 13.10: A video sequence (left) and the progressive (middle)) and (interlaced) scan formats.

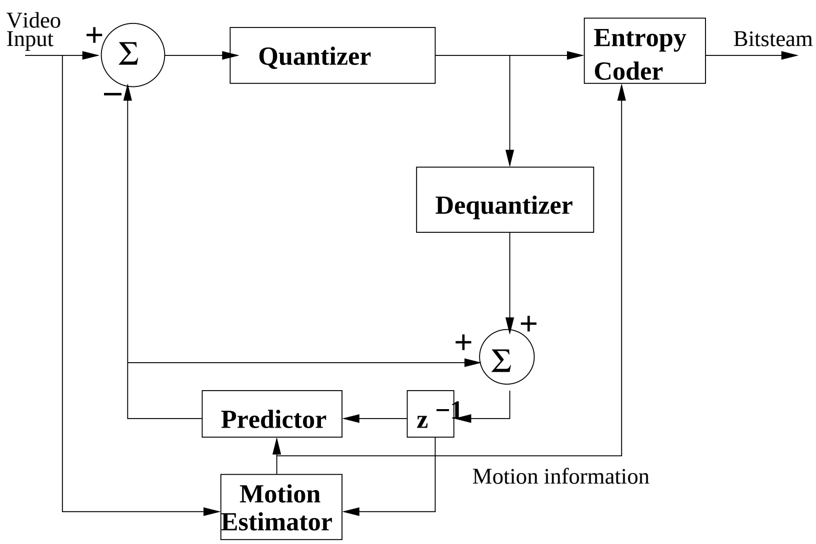

Figure 13.11: System for motion-compensated predictive coding (MCPC) between frames of a video sequence.

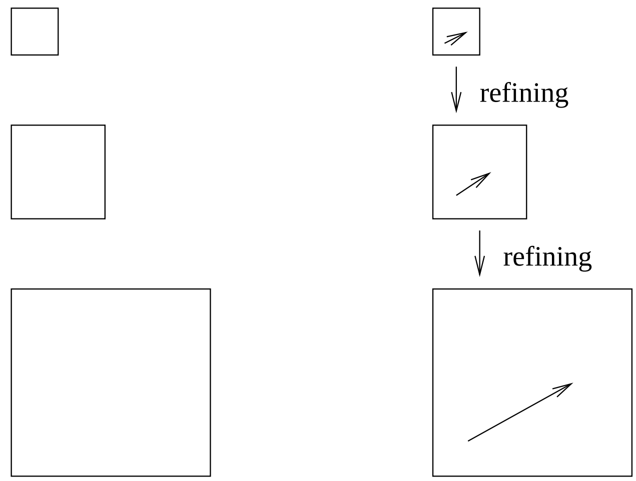

Figure 13.12: Hierarchical motion estimation in three scales.

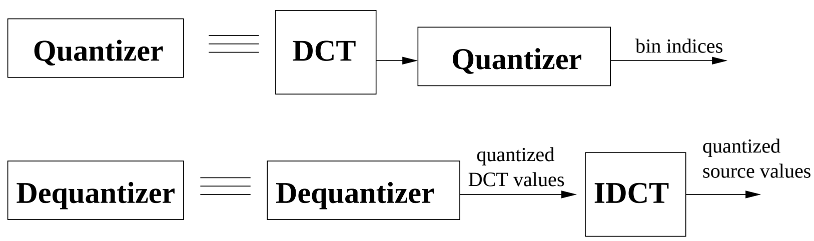

Figure 13.13: Quantizer and Dequantizer equivalences to transform types in MCPC loop.

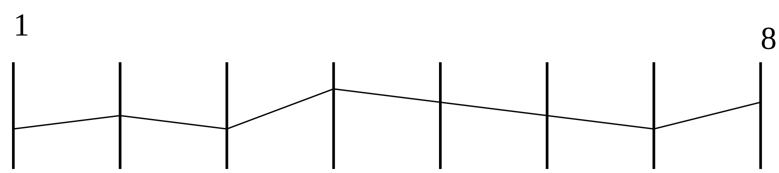

Figure 13.14: Side view of a motion thread through an 8-frame GOP.

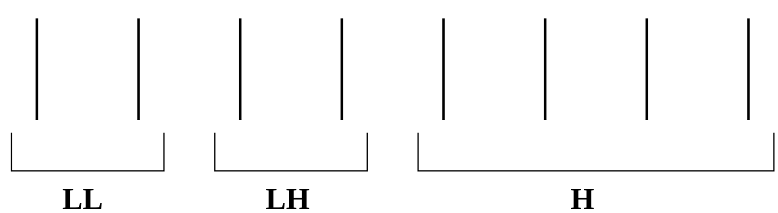

Figure 13.15: Temporal subbands of a two-level wavelet transform of an 8-frame GOP: LL = low-low; LH = low-high; H = high.

Chapter 14

Distributed Source Coding

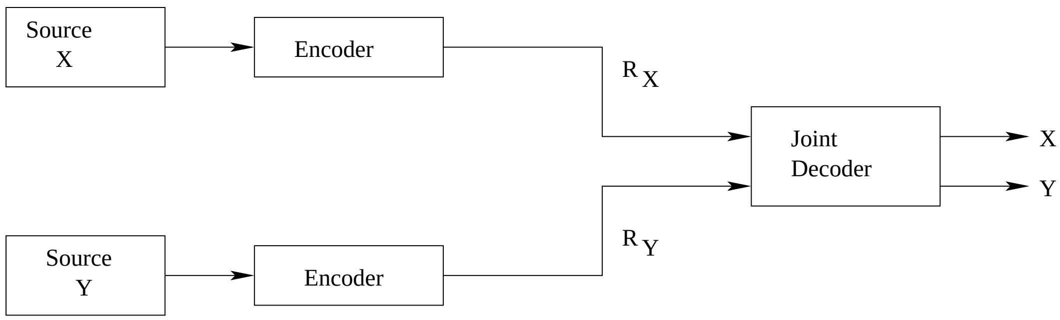

Figure 14.1: Distributed source coding: independent encoding and joint decoding of correlated sources.

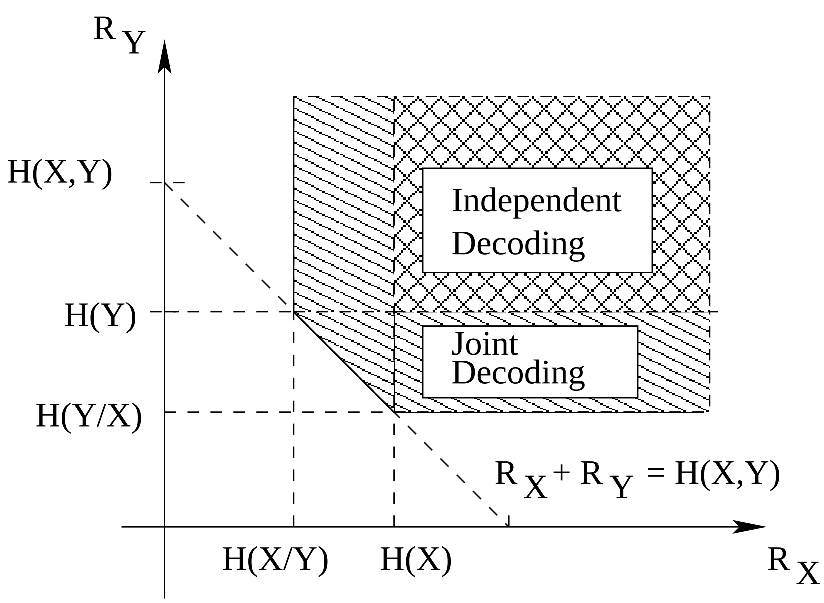

Figure 14.2: Rate regions for achieving lossless reconstruction for joint and independent decoding.

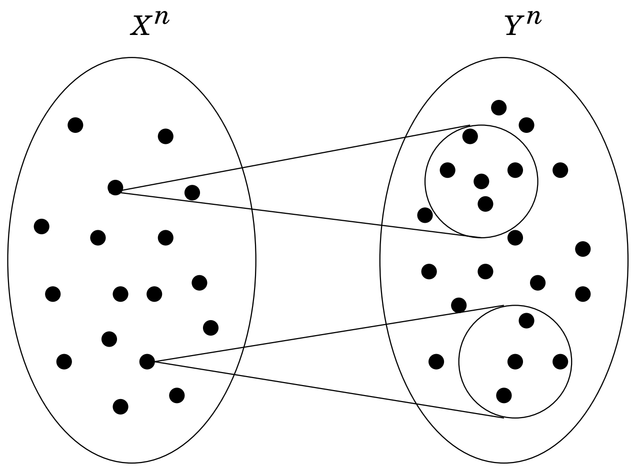

Figure 14.3: Fans of points in $\mathcal{Y}^n$ typically linked to points $\mathbf{x}$ in $\mathcal{X}^n$.

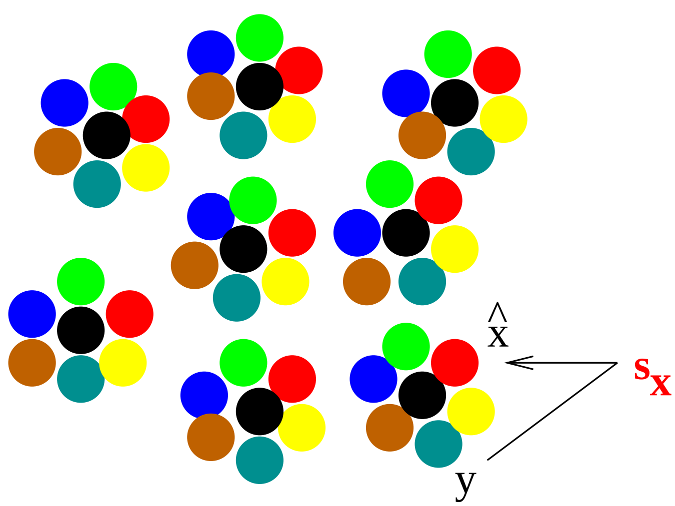

Figure 14.4: Illustration of correctable regions as clusters of balls and cosets as like-colored balls. Only the red color of $\mathbf{y}$ is known, so is indicated by the red color of its syndrome $\mathbf{s}_y$. Therefore, $\mathbf{y}$ is declared to be the red ball closest to $\mathbf{x}$ and is marked as $\hat{\mathbf{y}}$. (The blank spaces are there just to exaggerate the display of the clusters and are not to be interpreted as distances.)

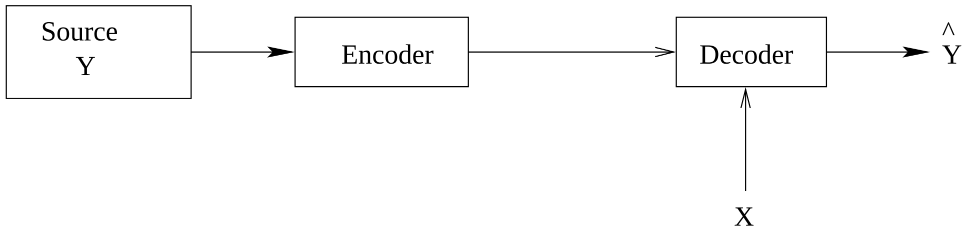

Figure 14.5: Source decoding with side information at the decoder.

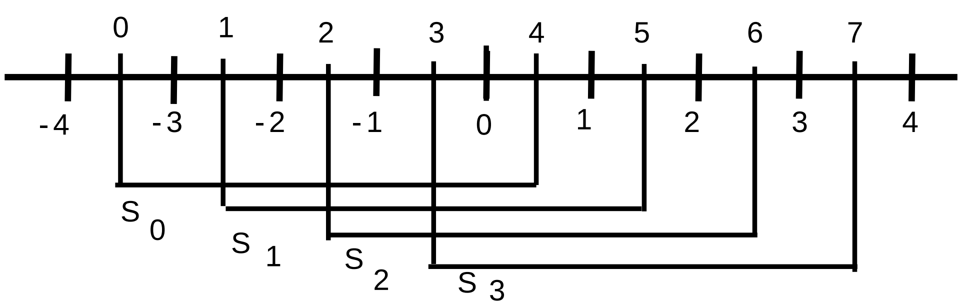

Figure 14.6: Quantization bins and cosets in scalar Wyner-Ziv uniform quantization ($R_s = 3, R_c = 1$).